

Electro-poroelastohydrodynamics of the endothelial glycocalyx layer and streaming potential in wavy-wall microvessels

C. Teodoro , J. Arcos , and O. Bautista *

ESIME Azcapotzalco, Instituto Politécnico Nacional, Avenida de las Granjas 682, Colonia Santa Catarina, Alcaldía Azcapotzalco, Ciudad de México 02250, Mexico

F. Méndez 

Departamento de Termofluidos, Facultad de Ingeniería, Universidad Nacional Autónoma de México, Alcaldía Coyoacán, Ciudad de México 04510, Mexico



(Received 13 August 2023; accepted 19 December 2023; published 16 January 2024)

In this work, we study a pressure-driven flow of a non-Newtonian electrolyte through a wavy microchannel whose walls are covered with an electrically charged poroelastic layer that models the endothelial glycocalyx layer (EGL). The focus of our work is on the analysis of the electrical and mechanical effects of pressure-driven flow and induced streaming potential. The electrolyte is a viscoelastic fluid that obeys the Phan-Thien-Tanner rheological model. The coupled equations that describe the dynamics of the fluid phase, the elastic EGL, and electric fields are solved asymptotically using the domain perturbation method for the wavy-wall microchannel. The governing equations are nondimensionalized, which depend on dimensionless parameters that characterize the physical phenomenon: the Weissenberg number Wi , the Hartmann number χ , the viscosity ratio μ_r of the fluid in the EGL (assumed as Newtonian) and in the lumen (assumed viscoelastic), and the dimensionless electric charge and thickness of the EGL, c_s and Λ , respectively. The viscoelastic fluid's shear stresses and induced streaming potential are lower in magnitude when compared to Newtonian fluids. According to the results, it may be possible to use the streaming potential as a biocompatible and safe energy source for different medical devices and biosensors.

DOI: [10.1103/PhysRevFluids.9.013101](https://doi.org/10.1103/PhysRevFluids.9.013101)

I. INTRODUCTION

Cardiovascular problems are the main cause of death in the world, which are not isolated problems but are related to other conditions such as arterial hypertension, cardiac arrhythmias, hypoxia, etc. In turn, these conditions are generally not treated on time since the symptoms only occasionally appear in the early stages of the conditions. For this reason, new ways have been sought to detect a disease at an early stage. There is a region that is currently of particular interest, which covers the inner walls of the heart and blood vessels and is known as the endothelial glycocalyx layer (EGL) and which is speculated to have a close relationship with the diseases mentioned above, which have direct effects on it from very early stages, such as reducing its volume by half.

The structure of a blood vessel is complex, but it can be summarized in the walls of the vessel or parenchyma, followed by the EGL and later the vascular lumen, which is the interior space of a tubular structure. Blood vessels range in diameter from 5 to 20 μm , with a basement membrane that supports endothelial cells. Endothelial cells are coated with the EGL, which is $\sim 20\text{--}500$ nm thick.

*Corresponding author: obautista@ipn.mx

This layer comprises many biomolecules such as glycolipids, glycoproteins, and proteoglycans, the last being a biomolecule with a negative electrical charge [1]. Among the functions that EGL is assumed to possess are the transduction of mechanical stress and regulation of vascular permeability. Additionally, it serves as a sieve for leukocytes and platelets, preventing them from adhering to or penetrating the endothelium. According to studies where the EGL is visualized, it has been appreciated that it does not have a constant thickness, and it has been shown that it is formed by a solid structure that allows the passage of a fluid through its components. Due to these two facts, one of the proposals when modeling its behavior is to consider EGL as a porous medium with no regular shape, which can also deform because it does not have a rigid structure [2].

The blood that flows through the blood vessels is formed by Na^+ and Cl^- ions immersed in the plasma and of different biological components (leukocytes, thrombocytes, and erythrocytes) that give it an electrolytic and viscoelastic behavior, provided that the diameter of the channels is sufficiently larger than the size of said biological components [3]. Since the endothelial wall is sensitive to stress and the EGL is a mechanotransduction layer, and these signals are converted into biochemical signals that directly relate to the individual's health, it is essential to understand which parameters can induce different stress configurations in the wall. The complex experimentation *in vivo* of the EGL has hindered studies in this field, giving a significant step to the physical-mathematical models that help to describe its behavior. However, some experimental studies have been developed [1,4]; therefore, analytical and especially numerical models remain the most studied.

Some studies of the EGL have considered the EGL as a rigid material [5]. Based on the above hypothesis, a biphasic mixing theory (BMT) can be proposed, which consists of modeling EGL as a porous and hydrated material composed of two phases (elastic solid, and liquid), this theory being the most widely used to describe the poroelastohydrodynamics of the EGL [3,6–9]. All these studies consider the EGL as an electrically neutral medium.

However, the EGL is not an electroneutral medium since one of its components, the proteoglycan, is a naturally charged macromolecule that causes EGL to be negatively charged; in addition, some theoretical studies suggest that the fixed charge concentration of EGL is of the same order of magnitude as the concentration of physiological neutral salt in the blood plasma (≈ 0.1 M) [10], so it is essential to analyze their electrical interactions. Some works that consider the electric charge of the EGL have used different models for the charge distribution, such as the charged surface model [11], the volumetric charge model [12], and a Mokady model [13,14]. For instance, the triphasic mixing theory (TMT) model can be used to describe the mechanical-electrical EGL behavior mathematically [15]. The result is a theoretical formulation consisting of a biphasic mixture with a complete solid matrix with fixed negative charges that interact with the electrolytic fluid that passes through its pores. In TMT theory, the fluid and solid phases are described by the modified Navier-Stokes equations, subject to electrical forces from the body.

Recently, Sumets *et al.* [16] presented a numerical study incorporating the simultaneous interaction between charged ions, a charged and deformable EGL, and a viscous fluid through the lumen, focusing on the stresses induced in the microchannel wall. On the other hand, Roy *et al.* [17] carried out an investigation dividing their study into three regions—the EGL, the lumen, and a coupling region between these two regions—using a non-Newtonian fluid for the lumen, the charged and porous EGL, focusing on the streaming potential. Until now, several works have taken different considerations but left aside others that may also be relevant. This work takes considerations that have been proposed so that it offers an approach to the actual phenomenon in comparison with other models and studies previously carried out according to the various conditions that medical studies have reported. The objective of this work is to understand how specific parameters related to the phenomenon affect the EGL, and a proposal from the literature is taken to consider an electrokinetic phenomenon that develops in the EGL as a possible source of biocompatible energy for medical devices.

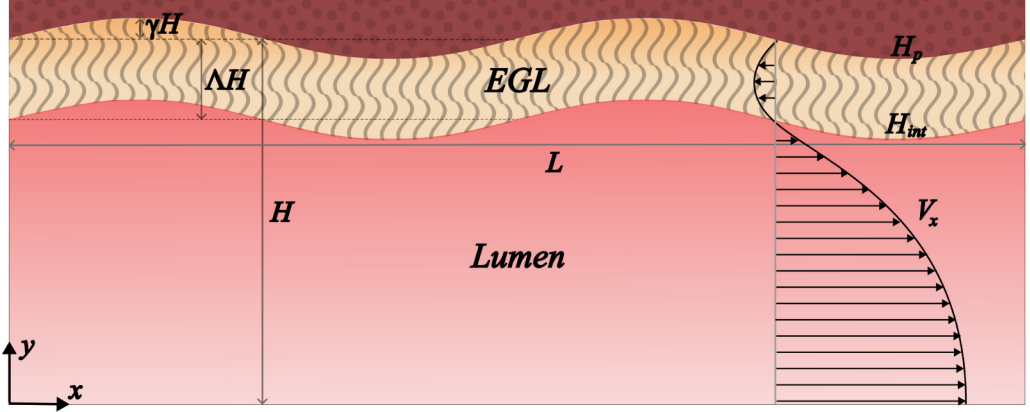


FIG. 1. Schematic of the two-dimensional physical model under study. Two regions are present, the lumen and the EGL, the latter assumed as an electrically charged poroelastic material. The interface between the lumen, the EGL, and the wall is wavy. Here, $H_{\text{int}}(x)$ and $H_p(x)$ represent the location of the lumen-EGL interface and EGL-microvessel wall, respectively. The thickness of the EGL is constant and, in its dimensional form, is represented as ΔH , where Δ is a parameter that indicates the fraction of the thickness of the EGL with respect to the microvessel half width. The amplitude of the undulations is represented by γH , and it is assumed that it is very small compared to H . V_x is a representative velocity profile.

II. SETUP AND PROBLEM FORMULATION

For the analysis, and following Refs. [7,16], we model the capillary blood vessel as a two-dimensional wavy-wall channel, as shown in Fig. 1. The physical domain is divided into two regions: the lumen and the EGL. The origin of the Cartesian coordinate system (x, y) is located in the center of the microchannel. The channel is considered very long with length L , with a mean width H , in such a way that $H/L \ll 1$. The walls and the lumen-EGL interface have a sinusoidal shape of the form

$$y = H_p(x) = H \left[1 + \gamma \sin \left(\frac{4\pi x}{L} \right) \right] \text{ and } H_{\text{int}}(x) = H \left[1 - \Delta + \gamma \sin \left(\frac{4\pi x}{L} \right) \right], \quad (1)$$

respectively.

For the analysis, and considering the symmetry with respect to the y axis, only half of the microchannel is studied. The wall is considered to be fixed and impermeable. The EGL is modeled as a poroelastic material composed of a fluid fraction ϕ_f and a solid fraction ϕ_s , which is also electrically charged. It is considered that the pores are interconnected, allowing the fluid to flow through the empty spaces. These cavities are large enough to be physically analyzed as global and average measurements as a conventional continuous medium, being also an isotropic material. This consideration is justified by the fact that $\phi_f \gg \phi_s$; that is, it is a material with very high porosity. On the other hand, the blood that flows through the blood vessels is modeled as a viscoelastic electrolyte that flows in the lumen and a Newtonian electrolyte in the EGL since it works as a molecular sieve of the components that give it a non-Newtonian behavior.

The fluid flow is produced by a constant pressure gradient, which has a value necessary for the blood to have a constant characteristic velocity $v_c \sim 10^{-3}$ m/s in the center of the channel [7]. There are no other types of external fields applied. A very long channel $H \ll L$ is considered, where L is a longitudinal characteristic length of $\sim 10^{-3}$ M for the smallest capillaries. Due to the physical dimensions of the phenomenon, it is considered a stationary flow, and the inertial and gravitational effects are neglected. Blood plasma is considered to be a dilute solution of water and ions. According to reported data [10,11], the concentration of ions in blood plasma is 0.1 mol l^{-1} . Under this consideration, the blood plasma fraction corresponding to ions is much smaller than

the corresponding water fraction, so ions can be considered point charges. A constant volumetric electric charge c_s , homogeneously distributed in the EGL is considered. We assume that, in the entire domain of the physical model, the sum of the charges is electrically neutral, and each component (anions, cations, ad EGL) generates its electric field that contributes to the total electric field. Neither chemical reactions nor temperature variations are considered.

The displacements in the EGL are determined from the small strain theory. Any changes in the electric field or in the shape of the interface that result from changes in the solid volume fraction are neglected; therefore, the solid and the fluid in the EGL are considered to be incompressible.

The research focuses on two main aspects, the determination of the streaming potential induced by the pressure gradient that originates the flow, and the shear stresses in the wall induced in the phenomenon so that the electric potential, the velocity fields, and displacements in the entire domain of study must be determined.

A. Governing and constitutive equations

1. Ionic distribution

Assuming that the potential due to the electrical double layer is independent of axial streaming potential in the microchannel (which is valid for long microchannels), one can write the total electric potential as $\Psi(x, y) = \psi(x, y) + (\phi_0 + xB_T^*(x))$, where ψ is the electric potential due to the electrical double layer, ϕ_0 is the value of the potential due to streaming potential at $x = 0$, and B_T^* is the streaming potential induced. The ionic distribution is assumed to behave according to the Boltzmann distribution:

$$c_i = C_{i0} \exp\left(-\frac{z_i e \psi}{k_B T}\right), \quad (2)$$

where c_i represents the ionic concentration under the presence of an electric potential ψ , C_{i0} is the ionic concentration in the electroneutral region, which occurs when $\psi = 0$, z_i is the ion valence, e is the elementary charge, k_B is the Boltzmann constant, T is the absolute temperature, and the subscript i represents the i th ionic species. Our study involves two ionic species, Na^+ and Cl^- , for which we have assigned the subscripts $i = +, -$ for simplicity.

2. Electric potential

The governing equation to determine the distribution of electric potential in this study corresponds to the Poisson equation, which is given by

$$\epsilon \nabla^2 \Psi = -\rho_f, \quad (3)$$

where ϵ represents a dielectric constant, ρ_f is the electric charge density, and $\nabla^2 \equiv (\partial^2/\partial x^2 + \partial^2/\partial y^2)$. Regarding ionic concentrations, the electrical charge density in the lumen can be written as $\rho_f = e(z_+ c_+ + z_- c_-)$. Furthermore, the electrolyte is symmetrical, where $|z_+| = |z_-| = z = 1$. Since it is an electroneutral electrolyte, $c_{+0} = c_{-0} = c_0$. For a microchannel of length $L \ll H$, the term $\partial^2(\phi_0 + xB_T^*)/\partial x^2$ in Eq. (3) may be neglected [18]. According to the Boltzmann distribution for the ionic concentration described in Eq. (2), Eq. (3) can be rewritten with the approximation of Gouy-Chapman theory. Based on Refs. [11,14], we assume low surface potentials in the wall or interface, i.e., $\psi_s \ll k_B T/e$, allowing to linearize Eq. (3). Therefore, the induced electric potential, ψ_L , for the lumen region is as follows:

$$\epsilon \nabla^2 \psi_L = \frac{2z^2 e^2 C_0}{k_B T} \psi_L. \quad (4)$$

Similarly, for the EGL, under the Gouy-Chapman theory and using the Debye-Hückel approximation, considering that in this region the charge density corresponds to $\rho_f = \phi_f e(z_+ c_+ + z_- c_-) +$

$\phi_s e z_s c_s$, the Gauss law for the fluid domain in the EGL is given by [16]

$$\epsilon \nabla^2 \psi_f = \phi_f \frac{2z_s^2 e^2 C_0}{k_B T} \psi_f - \phi_s z_s e c_s, \quad (5)$$

where z_s and c_s are the valence and electric charge in the EGL, respectively. The boundary conditions for Eqs. (4) and (5) are

$$\frac{\partial \psi_L}{\partial y} = 0 \quad \text{at } y = 0, \quad (6)$$

$$\psi_L = \psi_f, \quad \frac{\partial \psi_L}{\partial n} = \frac{\partial \psi_f}{\partial n} \quad \text{at } y = H_{\text{int}}(x), \quad (7)$$

and

$$\frac{\partial \psi_f}{\partial n} = 0 \quad \text{at } y = H_p(x), \quad (8)$$

where n is the normal coordinate to the interfaces $H_{\text{int}}(x)$ and $H_p(x)$. Equation (7) represents the continuity of electric potential under the assumption that there is only a volume charge distribution without any surface charge concentration and that both media have the same electrical permittivity.

3. Momentum and mass conservation

The momentum and mass conservation equations for the lumen are given by

$$\rho_L \frac{D\mathbf{v}_L}{Dt} = -\nabla p + \nabla \cdot \boldsymbol{\tau}_L - k_B T \nabla (c_{L+} + c_{L-}) - ez(c_{L+} - c_{L-}) \nabla \Psi_L, \quad (9)$$

and

$$\nabla \cdot \mathbf{v}_L = 0, \quad (10)$$

respectively. Here, \mathbf{v}_L represents the velocity vector with components v_{xL} and v_{yL} in the directions x and y , respectively. ρ_L is the fluid density in the lumen, p is the pressure scalar field, $\boldsymbol{\tau}_L$ is the viscous stress tensor in the lumen, and c_{L+} and c_{L-} are the ionic concentrations of the cation and anion in the lumen, respectively. The nabla operator is $\nabla \equiv (\partial/\partial x \mathbf{i}, \partial/\partial y \mathbf{j})$, with \mathbf{i} and \mathbf{j} representing the unit vectors in the x and y directions, respectively. In addition to the inertial and viscous terms, the momentum conservation equation considers the presence of terms for osmotic pressure and electric force due to concentration and electric potential gradients, respectively, since the fluid is an electrolyte and may be sensitive to such effects. For the EGL region, it is necessary to introduce Darcy's law model for the momentum equation [19]. The momentum and continuity conservation equations for the fluid phase in the EGL are as follows:

$$\phi_f \left(\rho_L \frac{D\mathbf{v}_f}{Dt} + \nabla p - \nabla \cdot \boldsymbol{\tau}_f + k_B T \nabla (c_{f+} + c_{f-}) + ez(c_{f+} - c_{f-}) \nabla \Psi_f \right) = -K \mathbf{v}_f, \quad (11)$$

and

$$\nabla \cdot \mathbf{v}_f = 0, \quad (12)$$

where K is the hydraulic resistivity, an empirical parameter that depends on the pore configuration and composition, and the fluid flowing through it. The subscript f refers to the fluid region, the fluid velocity vector is denoted by \mathbf{v}_f and the corresponding stress tensor is $\boldsymbol{\tau}_f$, and the ionic concentrations are represented by $c_{f\pm}$. On the other hand, for the solid phase, there is also a conservation-of-motion equation that involves elastic, electrical, and osmotic stresses and which, in turn, is coupled to the conservation-of-momentum equation of the fluid phase through $K \mathbf{v}_f$, which is the momentum that is transferred between both phases of the porous medium according to Darcy's model.

The governing equation for the solid phase is given by [16]

$$\phi_s[\nabla p - \nabla \cdot \boldsymbol{\tau}_s + k_B T \nabla(c_{f+} + c_{f-}) + e z_s c_s \nabla \Psi_f] = \mathbf{K} \mathbf{v}_f. \quad (13)$$

Here, $\boldsymbol{\tau}_s$ represents the stress tensor of the solid phase. The boundary conditions for Eqs. (9), (11), and (13) are

$$\frac{\partial \mathbf{v}_L}{\partial y} = 0 \quad \text{at } y = 0, \quad (14)$$

$$\mathbf{v}_L = \phi_f \mathbf{v}_f, \quad \boldsymbol{\tau}_L \cdot \mathbf{n} = \boldsymbol{\tau}_f \cdot \mathbf{n}, \quad \boldsymbol{\tau}_L \cdot \mathbf{n} = \boldsymbol{\tau}_s \cdot \mathbf{n} \quad \text{at } y = H_{\text{int}}(x), \quad (15)$$

and

$$\mathbf{v}_f = \mathbf{u} = 0 \quad \text{at } y = H_p(x), \quad (16)$$

where \mathbf{u} is the vector of displacements with components u_x and u_y in the directions x and y , respectively, and \mathbf{n} represents a unit vector normal to the surface. Equation (15) represents the continuity of velocity and stress, the latter defined by the corresponding constitutive equations of the Phan-Thien-Tanner model [20] described in the next section.

4. Constitutive equations

The fluid in the lumen region is assumed to be viscoelastic and to obey the Phan-Thien-Tanner rheological model. In this manner, the stress tensor is given by [20]

$$f(\tau_{kk_L}) \boldsymbol{\tau}_L + \lambda \left\{ \frac{D \boldsymbol{\tau}_L}{Dt} - [(\nabla \mathbf{v}_L)^T \cdot \boldsymbol{\tau}_L + \boldsymbol{\tau}_L \cdot (\nabla \mathbf{v}_L)] \right\} = \eta (\nabla \mathbf{v}_L + (\nabla \mathbf{v}_L)^T), \quad (17)$$

where λ is the relaxation time, and η represents the dynamic viscosity of the lumen. The function $f(\tau_{kk})$ is a trace function of the stress tensor described by the following relationship:

$$f(\tau_{kk_L}) = 1 + \frac{\varepsilon \lambda}{\eta} (\tau_{xx_L} + \tau_{yy_L}), \quad (18)$$

with ε representing an elongational parameter of the fluid. For the fluid phase of the EGL, according to what was previously mentioned, it is considered a Newtonian fluid, so the stress tensor corresponds to

$$\boldsymbol{\tau}_f = \mu_f [\nabla \mathbf{v}_f + (\nabla \mathbf{v}_f)^T], \quad (19)$$

where μ_f represents the viscosity of the blood plasma. For the solid phase, assuming the use of elastic theory under small deformations, the stress tensor is given by

$$\boldsymbol{\tau}_s = \mu_s [\nabla \mathbf{u} + (\nabla \mathbf{u})^T] + \lambda_s (\nabla \cdot \mathbf{u}) \mathbf{I}, \quad (20)$$

where μ_s and λ_s are the elastic parameters of Lamé, and \mathbf{I} is the identity matrix.

5. Electric current in the EGL

The streaming potential, according to its definition, is the electric potential that is induced by the movement of ions in a flow driven by a pressure gradient that connects two reservoirs with the same concentration of ions in such a way that a net electric current does not exist longitudinally. In this context, we need to evaluate the current density vector given by [21]

$$\mathbf{i}_e = e \mathbf{v}(c_+ - c_-) - e D_{\pm} \nabla c_{\pm} \mp \frac{z e^2 D_{\pm}}{kT} c_{\pm} \nabla \Psi. \quad (21)$$

Because it is assumed that there is no current through the channel wall, the current density i_{e-x} per unit width of the slit channel in the x direction in the EGL, from Eq. (21), is given by

$$i_{e-x} = \int_{H_{\text{int}}}^{H_p} \left[e v_x (c_+ - c_-) - e D_{\pm} \frac{\partial c_{\pm}}{\partial x} \mp \frac{z e^2 D_{\pm}}{kT} c_{\pm} \frac{\partial \Psi_f}{\partial x} \right] dy = 0. \quad (22)$$

In Eq. (22), the first, second, and third terms inside the integral correspond to the current density due to the fluid motion, ionic diffusion, and migration affected by the potential gradient, respectively. The streaming potential is induced to generate a streaming current (caused by the induced electric field) that counterbalances the conduction current (caused by the fluid flow) [22].

B. Dimensionless mathematical model

To nondimensionalize the governing equations, we use the following dimensionless variables:

$$\begin{aligned}
 \bar{y} &= \frac{y}{H}, & \bar{x} &= \frac{x}{L}, & \bar{v}_{Lx,fx} &= \frac{v_{Lx,fx}}{V_0}, & \bar{v}_{Ly,fy} &= \frac{v_{Ly,fy}L}{HV_0}, & \bar{\tau}_{L,f} &= \frac{\tau_{L,f}H}{\mu_f V_0}, \\
 \bar{\tau}_s &= \frac{\tau_s \Phi H}{\mu_f V_0}, & \bar{p}_{L,f} &= \frac{\rho H^2}{\mu_f V_0 L}, & \bar{\mathbf{u}} &= \frac{\mathbf{u} \Phi \mu_s}{V_0 \mu_f}, & \bar{c}_L &= \frac{c_L}{C_0}, \\
 \bar{c}_f &= \frac{c_f \phi_f}{C_0}, & \bar{c}_s &= \frac{c_s \phi_s |z_s|}{C_0}, & \bar{\psi}_{L,f} &= \frac{\psi z e}{k_B T}, & G_T &= \left(\frac{\partial p_{L,f}}{\partial x} \right) \frac{H^2}{\mu_f V}, \\
 B_T &= (B_T^*) \frac{eH}{k_B T}, & \bar{\mathbf{i}}_e &= \frac{\mathbf{i}_e}{V_0 C_0 H}.
 \end{aligned} \tag{23}$$

Here, G_T and B_T are the dimensionless pressure and electric potential gradients, respectively, which are of interest to our study, and we denote them as

$$G_T = G + G' \quad \text{and} \quad B_T = B + B'. \tag{24}$$

The above definitions of G_T and B_T result from the cross-section variations of the microchannel along the x direction, giving rise to an induced pressure gradient G' and another perturbation associated with the electric potential B' . G and B denote mean pressure and electric gradients. In Eq. (23), the characteristic lengths were chosen according to the dimensions of our study region, the longitudinal characteristic velocity V_0 corresponds to the average velocity of flow in the bloodstream, and the characteristic concentrations are scaled with C_0 , which corresponds to the concentration of ions in the blood plasma, c_∞ . For the stresses, displacements, electric potential, electrical current, and pressure and electric potential gradients, their characteristic values arise when comparing the order of magnitude between different terms of the governing equations.

1. Dimensionless equations for the electric potential

In the dimensionless mathematical model shown in Eqs. (26)–(47), the following parameters arise:

$$\begin{aligned}
 \beta &= \frac{H}{L}, & \text{Re} &= \frac{\rho V_0 H}{\mu_f}, & \chi &= \frac{C_0 k_B T H}{\mu_f V_0}, & \mu_r &= \frac{\mu_f}{\eta}, & \text{Pe}_\pm &= \frac{V_0 H}{D_\pm}, \\
 \text{Wi} &= \frac{V_0 \lambda}{H}, & \bar{\kappa} &= \left(\frac{2z C_0 e^2 H^2}{\epsilon k_B T} \right)^{1/2}, & \xi &= \frac{KH^2}{\eta \phi_f}, & \Phi &= \frac{\phi_s}{\phi_f}.
 \end{aligned} \tag{25}$$

Here, β is the aspect ratio, Re denotes the Reynolds number, the Hartmann number is χ , μ_r is the viscosity ratio between the Newtonian and viscoelastic fluids, Pe_\pm is the Péclet number of each ion, Wi is the Weissenberg number, the dimensionless inverse of the Debye length thickness is denoted by $\bar{\kappa}$, the inverse of Darcy's permeability ξ , and Φ is a relationship between the solid and fluid fracture of the porous medium.

The dimensionless forms of the Poisson-Boltzmann equations, Eqs. (4) and (5), are given by

$$-\left(\beta^2 \frac{\partial^2 \bar{\psi}_L}{\partial \bar{x}^2} + \frac{\partial^2 \bar{\psi}_L}{\partial \bar{y}^2} \right) = \frac{\bar{\kappa}^2}{2} (\bar{c}_{L+} - \bar{c}_{L-}), \tag{26}$$

and

$$-\left(\beta^2 \frac{\partial^2 \bar{\psi}_f}{\partial \bar{x}^2} + \frac{\partial^2 \bar{\psi}_f}{\partial \bar{y}^2}\right) = \frac{\bar{\kappa}^2}{2} (\bar{c}_{f+} - \bar{c}_{f-} - \bar{c}_s). \quad (27)$$

Here, the dimensionless ionic distributions, from Eq. (2), are defined as

$$\bar{c}_{L\pm} = \exp(\mp \bar{\psi}_L), \quad (28)$$

and

$$\bar{c}_{f\pm} = \exp(\mp \bar{\psi}_f). \quad (29)$$

2. Momentum and continuity dimensionless equations

The dimensionless form of the momentum and continuity equations, Eqs. (9) and (10), in the lumen region are the following:

$$\beta \text{Re} \left(\bar{v}_{xL} \frac{\partial \bar{v}_{xL}}{\partial \bar{x}} + \bar{v}_{yL} \frac{\partial \bar{v}_{xL}}{\partial \bar{y}} \right) = -G_T + \left(\beta \frac{\partial \bar{\tau}_{xxL}}{\partial \bar{x}} + \frac{\partial \bar{\tau}_{xyL}}{\partial \bar{y}} \right) - \beta \chi \left(\frac{\partial \bar{c}_{L+}}{\partial \bar{x}} + \frac{\partial \bar{c}_{L-}}{\partial \bar{x}} \right) - \chi \left[(\bar{c}_{L+} - \bar{c}_{L-}) \left(\beta \frac{\partial \bar{\psi}_L}{\partial \bar{x}} + B_T \right) \right], \quad (30)$$

$$\beta^2 \text{Re} \left(\bar{v}_{xL} \frac{\partial \bar{v}_{yL}}{\partial \bar{x}} + \bar{v}_{yL} \frac{\partial \bar{v}_{yL}}{\partial \bar{y}} \right) = -\frac{1}{\beta} \frac{\partial \bar{p}_L}{\partial \bar{y}} + \left(\beta \frac{\partial \bar{\tau}_{xyL}}{\partial \bar{x}} + \frac{\partial \bar{\tau}_{yyL}}{\partial \bar{y}} \right) - \chi \left(\frac{\partial \bar{c}_{L+}}{\partial \bar{y}} + \frac{\partial \bar{c}_{L-}}{\partial \bar{y}} \right) - \chi \left[(\bar{c}_{L+} - \bar{c}_{L-}) \frac{\partial \bar{\psi}_L}{\partial \bar{y}} \right], \quad (31)$$

and

$$\frac{\partial \bar{v}_{xL}}{\partial \bar{x}} + \frac{\partial \bar{v}_{yL}}{\partial \bar{y}} = 0. \quad (32)$$

For the EGL region, the corresponding dimensionless forms of Eqs. (11) and (12) are

$$\beta \text{Re} \left(\bar{v}_{xf} \frac{\partial \bar{v}_{xf}}{\partial \bar{x}} + \bar{v}_{yf} \frac{\partial \bar{v}_{xf}}{\partial \bar{y}} \right) = -G_T + \left(\beta \frac{\partial \bar{\tau}_{xxf}}{\partial \bar{x}} + \frac{\partial \bar{\tau}_{xyf}}{\partial \bar{y}} \right) - \beta \chi \left(\frac{\partial \bar{c}_{f+}}{\partial \bar{x}} + \frac{\partial \bar{c}_{f-}}{\partial \bar{x}} \right) - \chi \left[(\bar{c}_{f+} - \bar{c}_{f-}) \left(\beta \frac{\partial \bar{\psi}_f}{\partial \bar{x}} + B_T \right) \right] - \xi \bar{v}_{xf}, \quad (33)$$

$$\beta^2 \text{Re} \left(\bar{v}_{xf} \frac{\partial \bar{v}_{yf}}{\partial \bar{x}} + \bar{v}_{yf} \frac{\partial \bar{v}_{yf}}{\partial \bar{y}} \right) = -\frac{1}{\beta} \frac{\partial \bar{p}_f}{\partial \bar{y}} + \left(\beta \frac{\partial \bar{\tau}_{xyf}}{\partial \bar{x}} + \frac{\partial \bar{\tau}_{yyf}}{\partial \bar{y}} \right) - \chi \left(\frac{\partial \bar{c}_{f+}}{\partial \bar{y}} + \frac{\partial \bar{c}_{f-}}{\partial \bar{y}} \right) - \chi \left[(\bar{c}_{f+} - \bar{c}_{f-}) \frac{\partial \bar{\psi}_f}{\partial \bar{y}} \right] - \xi \bar{v}_{yf}, \quad (34)$$

and

$$\frac{\partial \bar{v}_{xf}}{\partial \bar{x}} + \frac{\partial \bar{v}_{yf}}{\partial \bar{y}} = 0. \quad (35)$$

Combining Eqs. (13) and (20), we obtain the the following dimensionless momentum equations for the solid region:

$$\beta \frac{\partial \bar{\tau}_{xxs}}{\partial \bar{x}} + \frac{\partial \bar{\tau}_{xys}}{\partial \bar{y}} = \Phi G_T + \Phi \beta \chi \left(\frac{\partial \bar{c}_{f+}}{\partial \bar{x}} + \frac{\partial \bar{c}_{f-}}{\partial \bar{x}} \right) - \chi \bar{c}_s \left(\beta \frac{\partial \bar{\psi}_f}{\partial \bar{x}} + B_T \right) - \xi \bar{v}_{xf}, \quad (36)$$

and

$$\beta \frac{\partial \bar{\tau}_{xyf}}{\partial \bar{x}} + \frac{\partial \bar{\tau}_{yyf}}{\partial \bar{y}} = \Phi \frac{1}{\beta} \frac{\partial \bar{p}_f}{\partial \bar{y}} + \Phi \chi \left(\frac{\partial \bar{c}_{f+}}{\partial \bar{y}} + \frac{\partial \bar{c}_{f-}}{\partial \bar{y}} \right) - \chi \bar{c}_s \frac{\partial \bar{\psi}_f}{\partial \bar{y}} - \xi \bar{v}_{xf}. \quad (37)$$

3. Dimensionless constitutive equations

The Phan-Thien-Tanner model (17) is recast in dimensionless form as follows:

$$\mu_r f(\bar{\tau}_{kkL}) \bar{\tau}_{xxL} + \mu_r \text{Wi} \left[\beta v_{xL} \frac{\partial \bar{\tau}_{xxL}}{\partial \bar{x}} + \beta v_{yL} \frac{\partial \bar{\tau}_{xxL}}{\partial \bar{y}} - 2 \left(\beta \bar{\tau}_{xxL} \frac{\partial \bar{v}_{xL}}{\partial \bar{x}} + \bar{\tau}_{xyL} \frac{\partial \bar{v}_{xL}}{\partial \bar{y}} \right) \right] = 2\beta \frac{\partial \bar{v}_{xL}}{\partial \bar{x}}, \quad (38)$$

$$\mu_r f(\bar{\tau}_{kkL}) \bar{\tau}_{yyL} + \mu_r \text{Wi} \left[\beta v_{xL} \frac{\partial \bar{\tau}_{yyL}}{\partial \bar{x}} + \beta v_{yL} \frac{\partial \bar{\tau}_{yyL}}{\partial \bar{y}} - 2 \left(\beta^2 \bar{\tau}_{xyL} \frac{\partial \bar{v}_{yL}}{\partial \bar{x}} + \beta \bar{\tau}_{yyL} \frac{\partial \bar{v}_{yL}}{\partial \bar{y}} \right) \right] = 2\beta \frac{\partial \bar{v}_{yL}}{\partial \bar{y}}, \quad (39)$$

and

$$\begin{aligned} \mu_r f(\bar{\tau}_{kkL}) \bar{\tau}_{xyL} + \mu_r \text{Wi} \left[\beta v_{xL} \frac{\partial \bar{\tau}_{xyL}}{\partial \bar{x}} + \beta v_{yL} \frac{\partial \bar{\tau}_{xyL}}{\partial \bar{y}} - \beta \bar{\tau}_{xyL} \left(\frac{\partial \bar{v}_{xL}}{\partial \bar{x}} + \frac{\partial \bar{v}_{yL}}{\partial \bar{y}} \right) - \beta^2 \bar{\tau}_{xxL} \frac{\partial \bar{v}_{yL}}{\partial \bar{x}} - \bar{\tau}_{yyL} \frac{\partial \bar{v}_{xL}}{\partial \bar{y}} \right] \\ = \beta^2 \frac{\partial \bar{v}_{yL}}{\partial \bar{x}} + \frac{\partial \bar{v}_{xL}}{\partial \bar{y}}, \end{aligned} \quad (40)$$

where $f(\bar{\tau}_{kkL})$ is the dimensionless form of the function of the trace of the stress tensor, given by

$$f(\bar{\tau}_{kkL}) = 1 + \mu_r \varepsilon \text{Wi} (\bar{\tau}_{xxL} + \bar{\tau}_{yyL}). \quad (41)$$

The fluid phase of the EGL is considered a Newtonian fluid, so the dimensionless stress tensor from Eq. (19) corresponds to

$$\bar{\tau}_{xxf} = 2\beta \frac{\partial \bar{v}_{xf}}{\partial \bar{x}}, \quad (42)$$

$$\bar{\tau}_{yyf} = 2\beta \frac{\partial \bar{v}_{yf}}{\partial \bar{y}}, \quad (43)$$

and

$$\bar{\tau}_{xyf} = \frac{\partial \bar{v}_{xf}}{\partial \bar{y}} + \beta \frac{\partial \bar{v}_{yf}}{\partial \bar{x}}. \quad (44)$$

For the solid phase, considering the constitutive equation (20), we obtain

$$\bar{\tau}_{xxs} = \left(2 + \frac{\lambda_s}{\mu_s} \right) \beta \frac{\partial \bar{u}_x}{\partial \bar{x}} + \frac{\lambda_s}{\mu_s} \frac{\partial \bar{u}_y}{\partial \bar{y}}, \quad (45)$$

$$\bar{\tau}_{yy_s} = \left(2 + \frac{\lambda_s}{\mu_s} \right) \beta \frac{\partial \bar{u}_y}{\partial \bar{y}} + \frac{\lambda_s}{\mu_s} \frac{\partial \bar{u}_x}{\partial \bar{x}}, \quad (46)$$

and

$$\bar{\tau}_{xys} = \frac{\partial \bar{u}_x}{\partial \bar{y}} + \beta \frac{\partial \bar{u}_y}{\partial \bar{x}}. \quad (47)$$

C. Asymptotic analysis in the asymptotic limit of $\beta \ll 1$ and $\text{Re} \ll 1$

According to the dimensionless parameters involved in the dimensionless mathematical model, Eqs. (26)–(47), it can be simplified based on the lubrication approximation [23]. Considering that in the phenomenon studied in this work, $\beta \ll 1$ and $\text{Re} \ll 1$ (see Table II), we can neglect $O(\beta)$, $O(\text{Re})$, $O(\beta \text{Re})$, and $O(\beta^2 \text{Re})$ terms. Therefore, the system of the dimensionless governing equations and boundary conditions in the leading order of the lubrication approximation can be written as follows.

TABLE I. Values of characteristic scales and physical constants involved in the work.

Parameter	Symbol	Value
Boltzmann constant	k_B	$1.38 \times 10^{-23} \text{ J K}^{-1}$
Elementary electric charge	e	1.610^{-19} C
Temperature	T	303.15 K
Electric permittivity of blood plasma [24]	ϵ	$6.78 \times 10^{-10} \text{ C}^2 (\text{N m}^2)^{-1}$
Plasma ionic concentration [16]	C_0	$0.154 \text{ mol l}^{-1} = 9.27 \times 10^{25} \text{ m}^{-3}$
Na ion diffusivity ($c_0 = 0.1 \text{ mol l}^{-1}$ and $T = 303.15 \text{ K}$) [16]	D_+	$1.62 \times 10^{-9} \text{ m}^2 \text{ s}^{-1}$
Cl ion diffusivity ($c_0 = 0.1 \text{ mol l}^{-1}$ and $T = 303.15 \text{ K}$) [16]	D_-	$2.45 \times 10^{-9} \text{ m}^2 \text{ s}^{-1}$
Plasma density	ρ	10^3 kg m^{-3}
Blood dynamic viscosity [11]	η	$3.5 \times 10^{-3} \text{ Pa s}$
Plasma dynamic viscosity	μ_f	$1.2 \times 10^{-3} \text{ Pa s}$
EGL shear modulus [25]	μ_s	6 kPa
Microchannel height	H	$5 \times 10^{-6} \text{ m}$
Microchannel length	L	10^{-3} m
Flow velocity [7]	V_0	10^{-3} m s^{-1}
Blood relaxation time [24]	λ	$\sim 7 \times 10^{-3} \text{ s}$
Fluid fraction	ϕ_f	0.99
Fluid extensibility	ϵ	0–1

(i) Poisson-Boltzmann equations:

$$-\frac{\partial^2 \bar{\psi}_L}{\partial \bar{y}^2} = \frac{\bar{\kappa}^2}{2} (\bar{c}_{L+} - \bar{c}_{L-}), \quad (48)$$

TABLE II. Dimensionless parameters' definitions and order of magnitude are estimated from values shown of physical parameters in Table I.

Parameter	Symbol	Value
Aspect ratio	$\beta = \frac{H}{L}$	$\sim 10^{-3}$
Reynolds number	$\text{Re} = \frac{\rho_0 V H}{\mu_f}$	$\sim 10^{-3}$
Hartmann number	$\chi = \frac{c_0 k_B T H}{\mu_f V}$	$\sim 10^6$
Péclet number (cation)	$\text{Pe}_+ = \frac{V H}{D_+}$	3
Péclet number (anion)	$\text{Pe}_- = \frac{V H}{D_-}$	2
Weissenberg number	$\text{Wi} = \frac{V \lambda}{H}$	$\sim 10^{-1}$
Inverse of Debye length	$\bar{\kappa} = \sqrt{\frac{c_0 e^2 H^2}{\epsilon k_B T}}$	$\sim 10^3$
Darcy permeability	$\xi = \frac{K H^2}{\phi_f \mu_f}$	$\sim 10^2$
Inverse of porosity	$\Phi = \frac{\phi_s}{\phi_f}$	$\sim 10^{-2}$
Viscosity ratio	$\mu_r = \frac{\mu_f}{\eta}$	$\sim 1/3$

and

$$-\frac{\partial^2 \bar{\psi}_f}{\partial \bar{y}^2} = \frac{\bar{\kappa}^2}{2} (\bar{c}_{f+} - \bar{c}_{f-} - \bar{c}_s), \quad (49)$$

with the boundary conditions

$$\frac{\partial \bar{\psi}_L}{\partial \bar{y}} = 0 \quad \text{at } \bar{y} = 0, \quad (50)$$

$$\bar{\psi}_L = \bar{\psi}_f, \quad \frac{\partial \bar{\psi}_L}{\partial n} = \frac{\partial \bar{\psi}_f}{\partial n} \quad \text{at } \bar{y} = \bar{H}_{\text{int}}(\bar{x}), \quad (51)$$

and

$$\frac{\partial \bar{\psi}_f}{\partial n} = 0 \quad \text{at } \bar{y} = \bar{H}_p(\bar{x}), \quad (52)$$

where $\bar{H}_{\text{int}}(\bar{x}) = \frac{H_p(\bar{x})}{H} = 1 - \Lambda + \gamma \sin(4\pi\bar{x})$ and $\bar{H}_p(\bar{x}) = \frac{H_p(\bar{x})}{H} = 1 + \gamma \sin(4\pi\bar{x})$ are the dimensionless interface and wall locations, respectively.

(ii) Momentum and mass conservation equations of the lumen region, starting from the fact that $\bar{c}_{L+} = \bar{c}_{L-}$ in this region:

$$G_T = \frac{\partial \bar{\tau}_{xyL}}{\partial \bar{y}}, \quad (53)$$

$$\frac{\partial \bar{p}_L}{\partial \bar{y}} = 0, \quad (54)$$

and

$$\frac{\partial \bar{v}_{xL}}{\partial \bar{x}} + \frac{\partial \bar{v}_{yL}}{\partial \bar{y}} = 0. \quad (55)$$

(iii) Momentum and mass conservation equations of the EGL region:

$$G_T = \frac{\partial \bar{\tau}_{xyf}}{\partial \bar{y}} - \chi(\bar{c}_{f+} - \bar{c}_{f-})B_T - \xi \bar{v}_{xf}, \quad (56)$$

and the following boundary conditions

$$\frac{\partial \bar{p}_f}{\partial \bar{y}} = 0, \quad (57)$$

$$\frac{\partial \bar{v}_{xf}}{\partial \bar{x}} + \frac{\partial \bar{v}_{yf}}{\partial \bar{y}} = 0. \quad (58)$$

(iv) Solid phase:

$$\frac{\partial \bar{\tau}_{xy_s}}{\partial \bar{y}} = \Phi G_T - \chi \bar{c}_s B_T - \xi \bar{v}_{xf}, \quad (59)$$

and

$$\frac{\partial \bar{p}_f}{\partial \bar{y}} = 0. \quad (60)$$

The boundary conditions for the dimensionless momentum conservation governing equations given in Eqs. (30) and (36) are the following:

$$\bar{v}_{xL} = 1, \quad \bar{\tau}_{xyL} = 0 \quad \text{at } \bar{y} = 0, \quad (61)$$

$$\bar{\mathbf{v}}_L = \phi_f \bar{\mathbf{v}}_f, \quad \bar{\boldsymbol{\tau}}_L \cdot \mathbf{n} = \bar{\boldsymbol{\tau}}_f \cdot \mathbf{n}, \quad \Phi \bar{\boldsymbol{\tau}}_L \cdot \mathbf{n} = \bar{\boldsymbol{\tau}}_s \cdot \mathbf{n} \quad \text{at } \bar{y} = \bar{H}_{\text{int}}(\bar{x}), \quad (62)$$

and

$$\bar{\mathbf{v}}_f = \bar{\mathbf{u}} = 0 \quad \text{at } \bar{y} = \bar{H}_p(\bar{x}). \quad (63)$$

1. Dimensionless constitutive stress equations

At the leading order of the lubrication approximation, the components of the dimensionless Phan-Thien-Tanner rheological model, from Eqs. (38)–(40), simplify as

$$\mu_r f(\bar{\tau}_{kkL}) \bar{\tau}_{xxL} - \mu_r 2Wi \bar{\tau}_{xyL} \frac{\partial \bar{v}_{xL}}{\partial \bar{y}} = 0, \quad (64)$$

$$\mu_r f(\bar{\tau}_{kkL}) \bar{\tau}_{yyL} = 0, \quad (65)$$

and

$$\mu_r f(\bar{\tau}_{kkL}) \bar{\tau}_{xyL} - \mu_r Wi \bar{\tau}_{yyL} \frac{\partial \bar{v}_{xL}}{\partial \bar{y}} = \frac{\partial \bar{v}_{xL}}{\partial \bar{y}}, \quad (66)$$

From Eq. (65), $\bar{\tau}_{yyL} = 0$, implying that the second term on the right-hand side of Eq. (66) disappears. Therefore, from Eqs. (64)–(66), we obtain a relationship between normal and shear stresses, $\bar{\tau}_{xxL} = 2\mu_r Wi \bar{\tau}_{xyL}^2$. For the fluid phase of the EGL, considered as a Newtonian fluid, the dimensionless stress tensor, based on Eq. (19), simplifies to

$$\bar{\tau}_{xyf} = \frac{\partial \bar{v}_{xf}}{\partial \bar{y}}. \quad (67)$$

For the solid phase, the dimensionless forms of the stresses, from Eq. (20), are given by

$$\bar{\tau}_{xxs} = \frac{\lambda_s}{\mu_s} \frac{\partial \bar{u}_y}{\partial \bar{y}}, \quad (68)$$

$$\bar{\tau}_{yys} = \frac{\lambda_s}{\mu_s} \frac{\partial \bar{u}_x}{\partial \bar{x}}, \quad (69)$$

and

$$\bar{\tau}_{xys} = \frac{\partial \bar{u}_x}{\partial \bar{y}}. \quad (70)$$

2. Dimensionless electric current in the EGL

The dimensionless electric longitudinal current induced by the flow of ions in the EGL region is given by

$$\bar{i}_{e-x} = \int_{\bar{H}_{\text{int}}}^{\bar{H}_p} \left(\bar{v}_{xf} (\bar{c}_+ - \bar{c}_-) \mp \frac{1}{\text{Pe}_{\pm}} \bar{c}_{\pm} B \right) d\bar{y}. \quad (71)$$

D. Asymptotic solution: Domain perturbation method

Considering that the EGL-lumen and EGL-capillary wall interfaces are wavy, whose relative positions are placed by using Eqs. (1), and if $\gamma \ll 1$, we proceed to use the domain perturbation method [23] to solve the formulated problem. Sumets *et al.* [16] used a dimensionless amplitude with respect to half the width of the microchannel of 0.02, which in our work corresponds to γ . Therefore, the following asymptotic expansion is proposed:

$$\Theta = \Theta_0 + \gamma \Theta_1 + O(\gamma^2). \quad (72)$$

In Eq. (72), Θ represents any variable of interest in this work, such as electric potential, stresses, velocities, and displacements in the lumen region and the EGL, where the subscript 0 represents the leading order that corresponds to the case of flat plates, and the subscript 1 represents the order γ that models the undulation of the interface and the wall. As $\gamma \ll 1$, terms of $O(\gamma^2)$ are neglected

in comparison with terms of $O(\gamma)$. Additionally, due to the wall's geometry change, the fluid must accelerate and decelerate, so an induced pressure gradient and streaming potential depend on the longitudinal position, to satisfy the mass and charge conservation. The pressure gradient G' and the streaming potential B' induced in the \bar{x} direction are of $O(\gamma)$ and, in terms of the asymptotic expansion (72), they are defined as

$$G' = \gamma G_{\text{ind}}(\bar{x}) + O(\gamma^2), \quad (73)$$

and

$$B' = \gamma B_{\text{ind}}(\bar{x}) + O(\gamma^2). \quad (74)$$

The domain perturbation method consists of transforming the boundary conditions at the wavy interfaces located at \bar{H}_p and \bar{H}_{int} to asymptotically equivalent boundary conditions applied at $\bar{y} = 1$ and at $\bar{y} = 1 - \Lambda$ [23]. The above is carried out by using a Taylor series for any dependent variable Θ at $\bar{y} = \bar{H}_p(\bar{x})$ and $\bar{y} = \bar{H}_{\text{int}}(\bar{x})$ in terms of Θ and its derivatives evaluated at $\bar{y} = 1$ and at $\bar{y} = 1 - \Lambda$ as follows:

$$\Theta|_{\bar{H}_p, \bar{H}_{\text{int}}} = \Theta|_{\bar{y}=1, 1-\Lambda} + \left(\frac{\partial \Theta}{\partial \bar{y}} \right)_{\bar{y}=1, 1-\Lambda} \gamma \sin(4\pi\bar{x}) + O(\gamma^2). \quad (75)$$

The solutions for the leading order and the $O(\gamma)$ of the asymptotic expansion are shown below. The leading-order solution represents the unidirectional phenomenon with flat walls. At this point it is useful to introduce a new spatial variable in the region of the EGL given by $y^* = 1 - \bar{y}$.

1. Ionic distribution

Typically, the largest magnitude of the electric potential is found in the EGL and is $\sim \bar{c}_s/2 \approx 1/2$ [16]. From Eqs. (28), (29), and (72) and linearizing terms in the form $\exp(x) \sim 1 + x + \dots$ based on the Debye-Hückel approximation, the ionic distributions can be written as

$$\bar{c}_{L\pm 0} \approx 1 \mp \bar{\psi}_{L0}, \quad (76)$$

$$\bar{c}_{f\pm 0} \approx 1 \mp \bar{\psi}_{f0}, \quad (77)$$

$$\bar{c}_{L\pm 1} \approx \mp \bar{\psi}_{L1}, \quad (78)$$

and

$$\bar{c}_{f\pm 1} \approx \mp \bar{\psi}_{f1}. \quad (79)$$

Equations (76)–(79) will be used to determine the electric current in Sec. IID 3 [see Eq. (94)].

2. Electric potential solution at $O(1)$

The dimensionless Poisson equation, Eq. (48) for the leading order, combined with Eq. (28), using the Debye-Hückel linearization, results in the following equation:

$$\frac{d^2 \bar{\psi}_{L0}}{d\bar{y}^2} = \bar{\kappa}^2 \bar{\psi}_{L0}. \quad (80)$$

Similarly, in the EGL region, the Poisson equation for the dimensionless electric potential for the leading order, combining Eqs. (49) and (29), is given by

$$\frac{d^2 \bar{\psi}_{f0}}{dy^{*2}} = \bar{\kappa}^2 \bar{\psi}_{f0} + \bar{\kappa}^2 \frac{\bar{c}_s}{2} \quad (81)$$

The dimensionless boundary conditions for Eqs. (80) and (81), according to Eqs. (50)–(52), are the following:

$$\frac{d\bar{\psi}_{L0}}{d\bar{y}} = 0 \quad \text{at } \bar{y} = 0, \quad (82)$$

$$\bar{\psi}_{L0} = \bar{\psi}_{f0}, \quad \frac{d\bar{\psi}_{L0}}{d\bar{y}} = \frac{d\bar{\psi}_{f0}}{d\bar{y}} \quad \text{at } \bar{y} = 1 - \Lambda, \quad (83)$$

and

$$\frac{d\bar{\psi}_{f0}}{d\bar{y}} = 0 \quad \text{at } \bar{y} = 1. \quad (84)$$

Solving Eqs. (80) and (81) yields

$$\bar{\psi}_{L0} = C_{pL} \cosh(\bar{\kappa}\bar{y}), \quad (85)$$

and

$$\bar{\psi}_{f0} = C_{pf} \cosh(\bar{\kappa}y^*) - \frac{\bar{c}_s}{2}, \quad (86)$$

whose constants are determined by applying the boundary conditions (82)–(84) and are shown in the Appendix.

3. Fluid velocity at $O(1)$

In the lumen region, combining Eq. (53) with Eqs. (64)–(66), the following equation is obtained:

$$(1 + 2\mu_r \varepsilon \text{Wi}^2 (G\bar{y})^2) \mu_r G \bar{y} = \frac{d\bar{v}_{xL0}}{d\bar{y}}. \quad (87)$$

The dimensionless momentum conservation equation of the leading order in the EGL region, according to Eqs. (28), (56), and (67), and using Debye-Hückel linearization, is given by

$$\frac{d^2 \bar{v}_{x_{f0}}}{dy^{*2}} = \xi \bar{v}_{x_{f0}} - 2B\chi C_{pf} \cosh(\bar{\kappa}y^*) + G + B\chi \bar{c}_s. \quad (88)$$

The dimensionless boundary conditions for the velocity, from Eqs. (61)–(63), for the leading order are

$$\frac{d\bar{v}_{xL0}}{d\bar{y}} = 0 \quad \text{at } \bar{y} = 0, \quad (89)$$

$$\bar{v}_{xL0} = \phi_f \bar{v}_{x_{f0}}, \quad \bar{\tau}_{xyL0} = \bar{\tau}_{xy_{f0}}, \quad \text{at } \bar{y} = 1 - \Lambda, \quad (90)$$

and

$$\bar{v}_{xL0} = 0 \quad \text{at } \bar{y} = 1. \quad (91)$$

Solving Eqs. (87) and (88), considering the boundary condition (89), the fluid velocity solutions are given by

$$\bar{v}_{xL0} = \frac{\mu_r G \bar{y}^2}{2} (1 + \varepsilon \text{Wi}^2 \mu_r^2 G^2 \bar{y}^2) + 1, \quad (92)$$

and

$$\bar{v}_{x_{f0}} = \left(-\frac{G + B\chi \bar{c}_s}{\xi} \right) + \frac{2B\chi C_{pf}}{\xi - \bar{\kappa}^2} \cosh(\bar{\kappa}y^*) + C_{f1} \exp(\sqrt{\xi}y^*) + C_{f2} \exp(-\sqrt{\xi}y^*). \quad (93)$$

C_{f1} and C_{f2} are constants of integration that will be determined together with G and B by applying the three boundary conditions shown in Eqs. (90) and (91) and the zero electric current condition in

the EGL. The electric current equation for the leading order, from Eq. (71), is

$$\bar{i}_e = \int_0^\Lambda \left[\bar{v}_{x_{f0}} (\bar{c}_{f0+} - \bar{c}_{f0-}) - B \left(\frac{\bar{c}_{f0+}}{\text{Pe}_+} + \frac{\bar{c}_{f0-}}{\text{Pe}_-} \right) \right] dy^* = 0. \quad (94)$$

By applying Eqs. (76)–(79), (90), (91), and (94), a system of nonlinear equations is obtained:

$$\begin{aligned} A_{11}G^3 + A_{12}G + A_{13}B + A_{14}C_{f1} + A_{15}C_{f2} &= -1, \\ A_{22}G + A_{23}B + A_{24}C_{f1} + A_{25}C_{f2} &= 0, \\ A_{32}G + A_{33}B + A_{34}C_{f1} + A_{35}C_{f2} &= 0, \\ A_{42}G + A_{43}B + A_{44}C_{f1} + A_{45}C_{f2} &= 0. \end{aligned} \quad (95)$$

The coefficients and the solution of the system of equations (95) are described in the Appendix.

4. EGL displacements at $O(1)$

The dimensionless momentum conservation equation at the leading order for the solid domain, according to Eqs. (59) and (70), is given by

$$\frac{d^2 \bar{u}_{x_0}}{dy^{*2}} = \Phi G - B\chi c_s - \xi \bar{v}_{x_{f0}}. \quad (96)$$

The dimensionless boundary conditions at the leading order, from Eqs. (61) and (63), are

$$\Phi \bar{v}_{ijL_0} = \bar{v}_{ij,s_0} \quad \text{at } \bar{y} = 1 - \Lambda, \quad (97)$$

and

$$\bar{u} = 0 \quad \text{at } \bar{y} = 1. \quad (98)$$

Substituting Eq. (93) in Eq. (96) and integrating yields

$$\begin{aligned} \bar{u}_{x_0} = & -\frac{2\xi B\chi C_{pf}}{\bar{\kappa}^2(\xi - \bar{\kappa}^2)} \cosh(\bar{\kappa}y^*) - C_{f1} \exp(\sqrt{\xi}y^*) - C_{f2} \exp(-\sqrt{\xi}y^*) + \frac{(\Phi + 1)}{2} Gy^{*2} \\ & + C_{u1}y^* + C_{u2}, \end{aligned} \quad (99)$$

where C_{u1}, C_{u2} are constants of integration, determined from Eqs. (97) and (98) and shown in the Appendix.

5. Electric potential solution at $O(\gamma)$

The Poisson-Boltzmann equation for the electric potential for the order γ , from Eq. (80), yields

$$\frac{\partial^2 \bar{\psi}_{L1}}{\partial \bar{y}^2} = \bar{\kappa}^2 \bar{\psi}_{L1}, \quad (100)$$

and in the EGL region, Eq. (81) can be written as

$$\frac{\partial^2 \bar{\psi}_{f1}}{\partial y^{*2}} = \bar{\kappa}^2 \bar{\psi}_{f1}. \quad (101)$$

At this order, the boundary conditions for the electric potential are

$$\frac{\partial \bar{\psi}_{L1}}{\partial \bar{y}} = 0 \quad \text{at } \bar{y} = 0, \quad (102)$$

$$\frac{\partial \bar{\psi}_{L1}}{\partial \bar{y}} - \frac{\partial \bar{\psi}_{f1}}{\partial \bar{y}} = \left(\frac{d^2 \bar{\psi}_{f0}}{d^2 \bar{y}} - \frac{d^2 \bar{\psi}_{L0}}{d^2 \bar{y}} \right) \sin(4\pi \bar{x}), \quad \bar{\psi}_{L1} = \bar{\psi}_{f1}, \quad \text{at } \bar{y} = 1 - \Lambda, \quad (103)$$

and

$$\frac{\partial \bar{\psi}_{f1}}{\partial \bar{y}} = -\frac{d^2 \bar{\psi}_{f0}}{d^2 \bar{y}} \sin(4\pi \bar{x}) \quad \text{at } \bar{y} = 1. \quad (104)$$

Solving Eqs. (100) and (101), the electric potential is obtained as follows:

$$\bar{\psi}_{L1} = C_{g1} \cosh(\bar{\kappa} \bar{y}), \quad (105)$$

and

$$\bar{\psi}_{f1} = C_{g2} \cosh(\bar{\kappa} y^*) + C_{g3} \sinh(\bar{\kappa} y^*). \quad (106)$$

The constants C_{g1} , C_{g2} , and C_{g3} are obtained by using the boundary conditions given in Eqs. (102)–(104), and shown in the Appendix.

6. Fluid velocity at $O(\gamma)$

The equation for conservation of momentum in the lumen for the order γ is obtained by combining Eqs. (53), (64), and (72), yielding

$$(1 + 6\varepsilon \text{Wi}^2 \mu_r^2 (G\bar{y})^2) \mu_r G_{\text{ind}} \bar{y} = \frac{\partial \bar{v}_{Lx1}}{\partial \bar{y}}. \quad (107)$$

Similarly, the momentum conservation equation for the fluid domain of the EGL at $O(\gamma)$ from Eqs. (56), (67), and (72), and using the Debye-Hückel linearization, results in

$$\frac{\partial^2 \bar{v}_{fx1}}{\partial y^{*2}} = \xi \bar{v}_{fx1} - 2\chi (B_{\text{ind}} C_{pf} + BC_{g2}) \cosh(\bar{\kappa} y^*) - 2B\chi C_{g3} \sinh(\bar{\kappa} y^*) + G_{\text{ind}} + B_{\text{ind}} \chi \bar{c}_s. \quad (108)$$

The boundary conditions for the fluid velocity at $O(\gamma)$ are

$$\bar{v}_{xL1} = \bar{\tau}_{xyL1} = 0 \quad \text{at } \bar{y} = 0, \quad (109)$$

$$\bar{v}_{xL1} - \bar{v}_{xf1} = \left(\frac{d^2 \bar{v}_{xf0}}{d\bar{y}^2} - \frac{d^2 \bar{v}_{xL0}}{d\bar{y}^2} \right) \sin(4\pi \bar{x}), \quad \text{and}$$

$$\bar{\tau}_{xyL1} - \bar{\tau}_{xyf1} = \left(\frac{d \bar{\tau}_{xyf0}}{d\bar{y}} - \frac{d \bar{\tau}_{xyL0}}{d\bar{y}} \right) \sin(4\pi \bar{x}) \quad \text{at } \bar{y} = 1 - \Lambda, \quad (110)$$

$$\bar{v}_{xf1} = -\frac{d \bar{v}_{xf0}}{d\bar{y}} \sin(4\pi \bar{x}) \quad \text{at } \bar{y} = 1. \quad (111)$$

Solving Eqs. (107) and (108), considering the boundary condition of Eqs. (109), the fluid velocity solutions are given by

$$\bar{v}_{Lx1} = \frac{\mu_r G_{\text{ind}} \bar{y}^2}{2} (1 + 3\mu_r^2 \varepsilon \text{Wi}^2 G^2 \bar{y}^2) + C_{g4}, \quad (112)$$

and

$$\bar{v}_{fx1} = \left(-\frac{G_{\text{ind}} + B_{\text{ind}} \chi \bar{c}_s}{\xi} \right) + \frac{2B\chi C_{g3}}{\xi - \bar{\kappa}^2} \sinh(\bar{\kappa} y^*) + \frac{2\chi (B_{\text{ind}} C_{pf} + BC_{g2})}{\xi - \bar{\kappa}^2}$$

$$\times \cosh(\bar{\kappa} y^*) + C_{g5} \exp(\sqrt{\xi} y^*) + C_{g6} \exp(-\sqrt{\xi} y^*). \quad (113)$$

The constants of integration, C_{g4} , C_{g5} , and C_{g6} , will be determined by applying the three boundary conditions shown in Eqs. (110) and (111). G_{ind} and B_{ind} are determined from the zero electric current

condition in the EGL in the γ order given by

$$\int_0^\Lambda \left\{ \bar{v}_{x_{f0}} (\bar{c}_{f1+} - \bar{c}_{f1-}) + \bar{v}_{x_{f1}} (\bar{c}_{f0+} - \bar{c}_{f0-}) - B \left(\frac{\bar{c}_{f1+}}{\text{Pe}_+} + \frac{\bar{c}_{f1-}}{\text{Pe}_-} \right) - B_{\text{ind}} \left(\frac{\bar{c}_{f0+}}{\text{Pe}_+} + \frac{\bar{c}_{f0-}}{\text{Pe}_-} \right) \right\} dy^* = 0, \quad (114)$$

together with the mass conservation condition. The mass conservation is based on the constraint that the volume flux must be independent of \bar{x} [23], i.e., $\int_0^1 v_x = \int_0^1 (v_{x_0} + \gamma v_{x_1} + O(\gamma^2)) = cte$, which implies that

$$\int_0^{1-\Lambda} \bar{v}_{x_{L1}} d\bar{y} + \int_{1-\Lambda}^1 \bar{v}_{x_{f1}} d\bar{y} = 0. \quad (115)$$

Substituting Eqs. (76)–(79), (93), and (113) and the B solution of Eq. (95) into Eq. (114) and Eqs. (112) and (113) into Eq. (115), it is possible to determine G_{ind} and B_{ind} solving numerically the following system of equations:

$$\int_0^{1-\Lambda} \bar{v}_{Lx10}(B_{\text{ind}0}, G_{\text{ind}0}, \bar{y}) d\bar{y} + \int_{1-\Lambda}^1 \bar{v}_{fx10}(B_{\text{ind}0}, G_{\text{ind}0}, \bar{y}) d\bar{y} = 0, \quad (116)$$

and

$$\int_{1-\Lambda}^1 \left(\bar{v}_{f0}(\bar{y})(\bar{c}_{f+10}(\bar{y}) - \bar{c}_{f-10}(\bar{y})) + \bar{v}_{fx10}(B_{\text{ind}0}, G_{\text{ind}0}, \bar{y})(\bar{c}_{f0+}(\bar{y}) - \bar{c}_{f0-}(\bar{y})) - B \left(\frac{\bar{c}_{f+10}(\bar{y})}{\text{Pe}_+} + \frac{\bar{c}_{f-10}(\bar{y})}{\text{Pe}_-} \right) - B_{\text{ind}0} \left(\frac{\bar{c}_{f0+}(\bar{y})}{\text{Pe}_+} + \frac{\bar{c}_{f0-}(\bar{y})}{\text{Pe}_-} \right) \right) d\bar{y} = 0, \quad (117)$$

where the γ -order solutions that depend on \bar{y} and \bar{x} were separated in the form $f(\bar{y}) \sin 4\pi \bar{x}$ to facilitate numerical calculation. Hence, $\bar{v}_{Lx10}(\bar{y})$, $\bar{v}_{fx10}(\bar{y})$, $\bar{c}_{f+10}(\bar{y})$, and $\bar{c}_{f-10}(\bar{y})$ are the independent part of \bar{x} from $\bar{v}_{Lx1}(\bar{y}, \bar{x})$, $\bar{v}_{fx1}(\bar{y}, \bar{x})$, $\bar{c}_{f+1}(\bar{y}, \bar{x})$, and $\bar{c}_{f-1}(\bar{y}, \bar{x})$, respectively, and are defined in the Appendix. Similarly, $B_{\text{ind}0}$ and $G_{\text{ind}0}$ are independent of \bar{x} . Therefore, B_{ind} and G_{ind} are given by

$$B_{\text{ind}} = B_{\text{ind}0} \sin(4\pi \bar{x}), \quad (118)$$

and

$$G_{\text{ind}} = G_{\text{ind}0} \sin(4\pi \bar{x}). \quad (119)$$

7. EGL displacements at $O(\gamma)$

The momentum conservation equation for the solid phase at $O(\gamma)$ from the substitution of the expansion proposed in Eq. (72) for \bar{u}_x and Eqs. (73), (74), and (113) in Eqs. (59) and (70) yields

$$\begin{aligned} \frac{\partial^2 \bar{u}_{x_1}}{\partial y^{*2}} &= (\Phi + 1)G_{\text{ind}} - \frac{2\chi\xi(B_{\text{ind}}C_{pf} + BC_{g2})}{\xi - \bar{\kappa}^2} \cosh(\bar{\kappa}y^*) \\ &\quad - \frac{2B\chi\xi C_{g3}}{\xi - \bar{\kappa}^2} \sinh(\bar{\kappa}y^*) - \xi C_{g5} \exp(\sqrt{\xi}y^*) - \xi C_{g6} \exp(-\sqrt{\xi}y^*). \end{aligned} \quad (120)$$

The dimensionless boundary conditions at the γ order, from Eqs. (61) and (63), are

$$\bar{\tau}_{xy_{x1}} - \Phi \bar{\tau}_{xy_{L1}} = \left(\Phi \frac{d\bar{\tau}_{xy_{L0}}}{d\bar{y}} - \frac{d\bar{\tau}_{xy_{s0}}}{d\bar{y}} \right) \sin(4\pi \bar{x}) \quad \text{at } \bar{y} = 1 - \Lambda, \quad (121)$$

and

$$\bar{u}_{x_1} = -\frac{d\bar{u}_{x_0}}{d\bar{y}} \sin(4\pi \bar{x}) \quad \text{at } \bar{y} = 1. \quad (122)$$

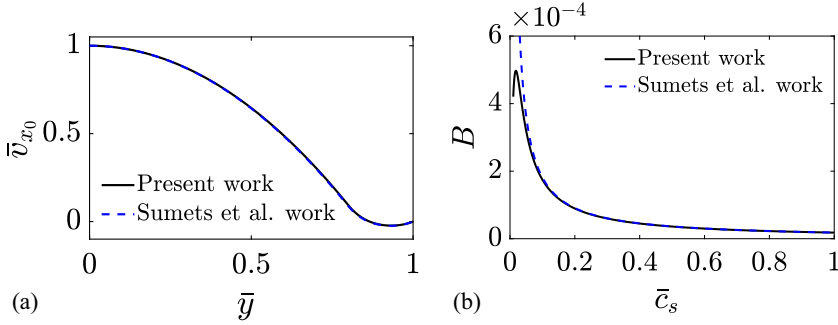


FIG. 2. Comparison of velocity profiles and streaming potential obtained in this work and those obtained by Sumets *et al.* [16]. With the nomenclature of this work, the results were obtained using $\Lambda = 0.2$, $\Phi = 0.01$, $\chi = 10^6$, $\bar{c}_s = 1$, $\xi = 250$, $\varepsilon \text{Wi}^2 = 0$, $\mu_r = 1$, and $\bar{\kappa} = 500$.

Solving Eq. (120), the distribution of the displacements at $O(\gamma)$ is given by

$$\begin{aligned} \bar{u}_{x_1} = & \frac{(\Phi + 1)}{2} G_{\text{ind}} y^{*2} - \frac{2\chi\xi(B_{\text{ind}}C_{pf} + BC_{g2})}{\bar{\kappa}^2(\xi - \bar{\kappa}^2)} \cosh(\bar{\kappa}y^*) \\ & - \frac{2B\chi\xi C_{g3}}{\bar{\kappa}^2(\xi - \bar{\kappa}^2)} \sinh(\bar{\kappa}y^*) - C_{g5} \exp(\sqrt{\xi}y^*) - C_{g6} \exp(-\sqrt{\xi}y^*) + C_{g7}y^* + C_{g8}. \end{aligned} \quad (123)$$

The constants C_{g7} and C_{g8} are obtained by applying the boundary conditions of Eqs. (121) and (122), and are shown in the Appendix.

III. RESULTS AND DISCUSSION

In this section, we discuss the influence that the asymptotic solution of the electric potential and velocity and displacement fields has on the stresses and the streaming potential induced. Besides, the effect of various parameters as well as the undulations of the wall are analyzed. Table I shows the typical values of constants and physical values used in the problem. Based on these values, Table II shows the dimensionless parameters described in the previous section, which result from deriving the corresponding dimensionless governing and constitutive equations.

To validate the asymptotic solution, we compare our results against those reported by Sumets *et al.* [16], who analyzed numerically the stresses in the wavy wall for a triphasic mixture of a Newtonian fluid. Their numerical solution is based on a coupled boundary element method–finite element method scheme. They also have added the approximate solutions for a flat channel, which are used directly to compare with ours. For this, it is necessary to consider the solution of our work of the leading order, i.e., that obtained with flat walls and interfaces, for a same Newtonian fluid in both regions ($\mu_r = 1$, $\varepsilon \text{Wi}^2 = 0$), and $\bar{\kappa} \rightarrow \infty$, since they are part of the considerations of the work by Sumets *et al.* [16]. Figure 2(a) shows the velocity profiles obtained from both studies which offer practically identical behavior. In contrast, Fig. 2(b) shows the streaming potentials induced in the phenomenon, which have the same behavior for values larger than $\bar{c}_s = 0.1$, since for lower values, the solution of Sumets *et al.* [16] is indeterminate, because it assumes $\bar{\kappa} \rightarrow \infty$. The above means that the Debye length is very small compared to the width of the microchannel, without resolving the boundary layer at the interface, giving a noncontinuous jump in the electric potential of the commented region. The comparison of these works provides confidence in our results. Some significant results that were obtained in this work are presented below.

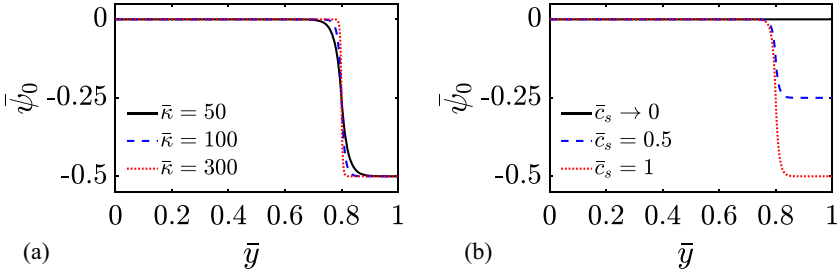


FIG. 3. Electric potential of the leading order for different configurations of parameters, with a value of $\Lambda = 0.2$: (a) several values of $\bar{\kappa}$ with $\bar{c}_s = 1$ and (b) varying the values of \bar{c}_s with $\bar{\kappa} = 100$.

A. Electric potential

Figure 3(a) shows the variation of ψ_0 as a function of the dimensionless coordinate \bar{y} for three different values of $\bar{\kappa}$ ($= 50, 100, 300$). It is shown that the larger value of $\bar{\kappa}$ yields larger potential gradients at the interface because the Debye length is smaller, generating a boundary layer at the interface. Figure 3(b) shows the dependence of ψ_0 on the coordinate \bar{y} for \bar{c}_s ($= 0, 0.5, 1$). The condition $\bar{c}_s \rightarrow 0$ is written in this way since the solution obtained remains indeterminate for the particular case of $\bar{c}_s = 0$, which allows us to recover the case in which the electrical effects in the phenomenon are neglected. The effect of the charge on the EGL is directly reflected in the magnitude of the electric potential in that region, which is to be expected since if there is no electric charge on the EGL, there are no electric fields generated by the movement of the electrolyte.

B. Flow velocity

The velocity field that develops in the phenomenon depends on different parameters: the viscosity ratio μ_r , the viscoelastic effect εWi^2 , the electrical effect \bar{c}_s , the permeability ξ , and the amplitude of the undulations, γ . Figure 4(a) shows the viscoelastic effect in the velocity profiles. It can be seen that, in the region of the lumen, viscoelasticity induces more significant velocity gradients near the EGL, which can be seen mathematically in Eq. (87), where the velocity gradients given by $\mu_r(1 + 2\varepsilon Wi^2(\mu_r G\bar{y})^2)G\bar{y}$ are larger compared to the gradients for the Newtonian case ($\varepsilon Wi^2 = 0$) given by $\mu_r G\bar{y}$, which is consistent with shear thinning exhibited by non-Newtonian fluids. The case $\varepsilon Wi^2 \rightarrow 0$ is included, which corresponds to the Newtonian case. Figure 4(b) shows the viscosity ratio effect on the velocity profiles. For lower values of μ_r , which mean higher viscosities in the lumen than that of the fluid phase in the EGL, a larger velocity magnitude at the interface and a greater magnitude of the reversed velocity in the EGL are observed. Figure 5(a) shows the effect of the dimensionless electric charge \bar{c}_s on the EGL, which is mainly reflected in the EGL region.

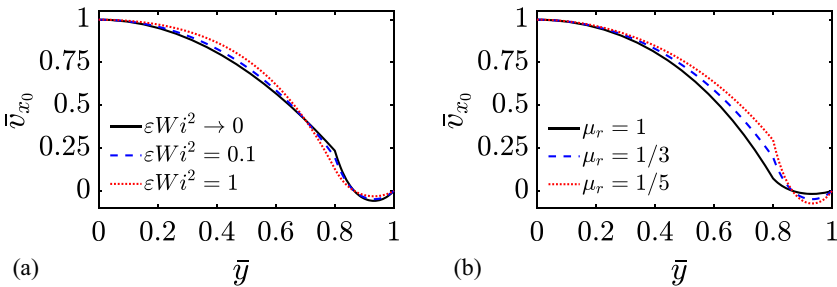


FIG. 4. Velocity profiles with $\Lambda = 0.2$, $\bar{c}_s = 1$, $\bar{\kappa} = 100$, $\xi = 250$, $\Phi = 0.01$, and $\chi = 10^6$: (a) εWi^2 ($= 0, 0.1, 1$) with $\mu_r = 1/3$ and (b) μ_r ($= 1, 1/3, 1/5$) with $\varepsilon Wi^2 = 0.1$.

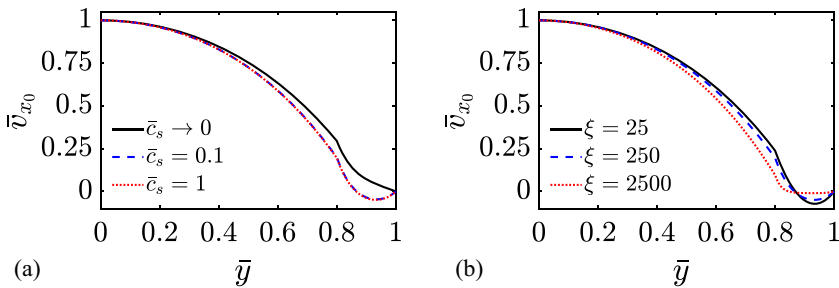


FIG. 5. Velocity profiles with $\varepsilon\text{Wi}^2 = 0.1$, $\Lambda = 0.2$, $\bar{\kappa} = 100$, $\mu_r = 1/3$, $\Phi = 0.01$, and $\chi = 10^6$ for (a) various values of \bar{c}_s ($= 0, 0.1, 1$) with $\xi = 250$, and (b) varying values of ξ ($= 25, 250, 2500$) with $\bar{c}_s = 1$.

An interesting phenomenon previously reported in other works [16,17] can be observed, which is a reversed flow in the EGL, which arises so that the net electric current is zero. Equation (94) is a null electric current condition in the EGL and it establishes that the electric current is related to the diffusion of ions in the EGL, and is divided into two parts: a convective diffusion $\bar{v}_{xj_0}(\bar{c}_{f0+} - \bar{c}_{f0-})$ and another electric diffusion $B(\frac{\bar{c}_{f0+}}{\text{Pe}_+} + \frac{\bar{c}_{f0-}}{\text{Pe}_-})$, physically necessary to balance the diffusion in such a way that the electric current is zero and reversed velocities are induced. On the other hand, for the case $\bar{c}_s \rightarrow 0$, which is the case where the electrical effect of the phenomenon is neglected, said return fluxes are not present. The effect of permeability is analyzed in Fig. 5(b). The parameter ξ represents the inverse of the permeability, and its effect is related to the velocity in the EGL since, for low permeabilities, the fluid does not manage to flow freely, unlike what has been shown for higher permeabilities. Velocity gradients are also affected by the permeability of the EGL since, for lower permeabilities, these gradients are smaller.

Figure 6 shows a case of velocity contours, where the velocity variation due to the wavy geometry can be observed. In the region where the channel narrows, the velocities obtained are higher due to the continuity of the fluid flow. Velocity gradients are the largest in the lumen region close to the interface. How the velocity contours are distributed has a larger amplitude in the region close to the microchannel's center than in the interface region.

C. Displacements in the EGL

The displacements in the EGL depend on different parameters such as the viscosity ratio μ_r , the viscoelastic effect εWi^2 , the electrical effect \bar{c}_s , the permeability ξ , and the effect of undulations, γ . Since $\bar{u}_x \sim O(1)$, i.e., $u_x \sim u_c \sim 10^{-8}$ M, while the thickness of the EGL is $\sim 10^{-6}$ M, according to the values reported in Table I, which means, the volume changes around $\sim 1\%$, the compression

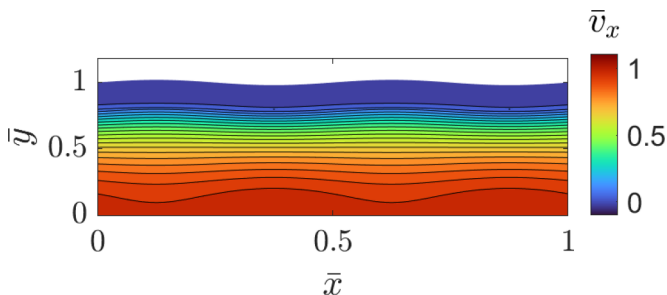


FIG. 6. Velocity contours for values of $\varepsilon\text{Wi}^2 = 0.1$, $\Lambda = 0.2$, $\bar{c}_s = 1$, $\bar{\kappa} = 100$, $\xi = 250$, $\Phi = 0.01$, $\chi = 10^5$, $\mu_r = 1$, and $\gamma = 0.02$.

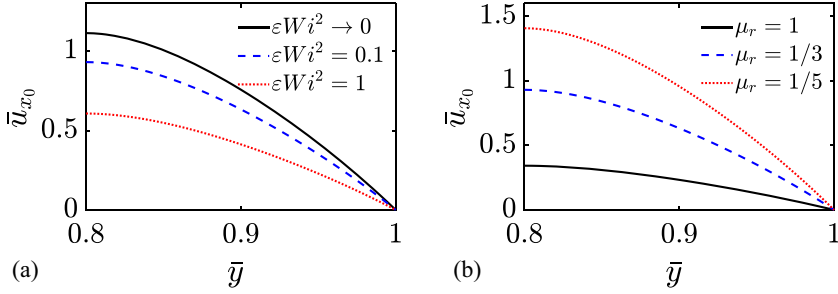


FIG. 7. EGL displacements with $\Lambda = 0.2$, $\bar{c}_s = 1$, $\bar{\kappa} = 100$, $\xi = 250$, $\Phi = 0.01$, and $\chi = 10^6$ for (a) $\epsilon Wi^2 (= 0, 0.1, 1)$ with $\mu_r = 1/3$ and (b) $\mu_r (= 1, 1/3, 1/5)$ with $\epsilon Wi^2 = 0.1$.

effects on the fluid are negligible as originally proposed. Figure 7(a) shows the viscoelastic effect in displacements. Unlike the effect on the velocity in the EGL, it does have a considerable impact on the magnitude of the displacements and deformations of the solid phase of the EGL, which can be explained physically because these displacements are a response to the shear stresses that are transmitted by fluid in the lumen, which vary with ϵWi^2 due to the shear thinning it presents. The viscoelastic fluid reduces the stresses in the interface compared to the Newtonian case, and these stresses are transmitted to the solid phase so that there are larger displacements in the interface for the Newtonian case. Figure 7(b) shows the viscosity ratio effect on displacements. For lower values of μ_r , a larger magnitude of the displacements at the interface is observed. The effect of the dimensionless electric charge of the EGL on the displacements is shown in Fig. 8(a). When the electrical effects are neglected ($\bar{c}_s = 0$), lower displacements are obtained because the electrical stresses in Eq. (96) affect the displacements. The permeability effect is analyzed in Fig. 8(b), which has a less significant effect on the magnitude of displacements than viscoelasticity, since displacements are defined by stress coupling at the interface, on which permeability does not have a significant effect. For higher permeabilities, smaller displacements are obtained at interface. Finally, Fig. 9 shows a case of displacement contours, where the variation of displacements due to undulations of the interfaces can be observed. The deformations are most remarkable in the region close to the wall.

D. Streaming potential

The induced streaming potential is independent of its transverse location in the microchannel, but its value varies longitudinally under corrugated walls. Figure 10(a) shows the variation of B as a function of ϵWi^2 . For the Newtonian case, the highest streaming potentials are obtained compared

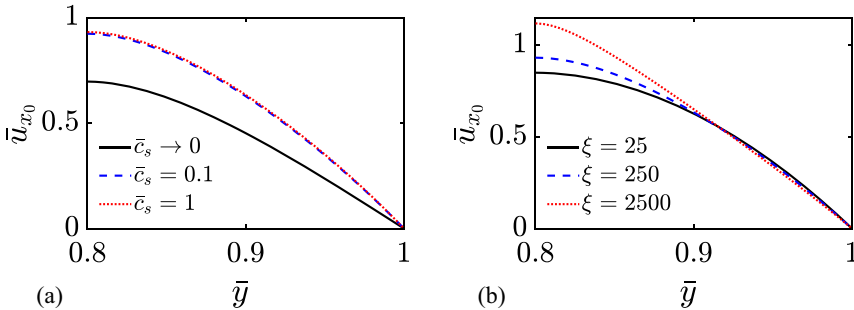


FIG. 8. EGL displacements using $\epsilon Wi^2 = 0.1$, $\Lambda = 0.2$, $\bar{\kappa} = 100$, and $\Phi = 0.01$, $\chi = 10^6$, $\mu_r = 1/3$ for (a) various values of \bar{c}_s and $\xi = 250$ and (b) varying the values of $\xi = (25, 250, 2500)$ with $\bar{c}_s = 1$.

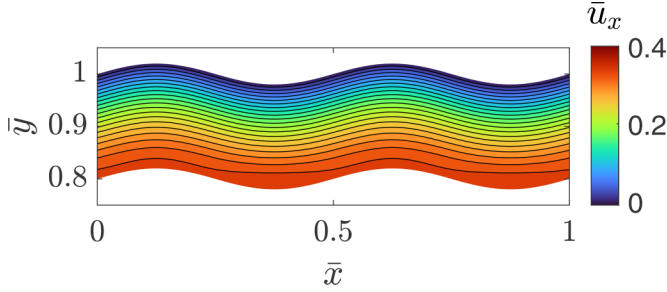


FIG. 9. Displacement contours in the solid phase of the EGL for values of $\varepsilon Wi^2 = 0.1$, $\Lambda = 0.2$, $\bar{c}_s = 1$, $\bar{\kappa} = 100$, $\xi = 250$, $\mu_r = 1$, $\Phi = 0.01$, $\chi = 10^5$, and $\gamma = 0.02$.

to those obtained when εWi^2 grows. The above can be explained if we analyze Fig. 4(a) since the magnitude of the velocities in the EGL for viscoelastic fluids is lower compared to Newtonian fluids, which is also due to the shear thinning of the viscoelastic fluid that reduces the stresses that are transmitted at the interface compared to a Newtonian fluid. Because B is induced to counteract the generated convective electric current, due to the movement of ions in this region, higher velocities induce a higher streaming potential. Figure 10(a) shows the streaming potential induced for different values of μ_r . When the viscosity in the lumen is considerably higher than that of the EGL, that is, lower values of μ_r , the streaming potential is more significant.

On the other hand, Fig. 10(b) shows the variation of B as a function of \bar{c}_s , and three values of the Hartmann number $\chi (= 5 \times 10^5, 10^6, 5 \times 10^6)$. For the case $\bar{c}_s \rightarrow 0$, the flow potential tends to zero because, without the electrical effects of the EGL, the concentrations of anions and cations are the same throughout the channel, and therefore there is no convective electric current and the presence of B is not necessary to counteract it. As the value of \bar{c}_s increases, the value of B increases until it reaches a point where its value begins to decrease again. The increase can be explained because the electric charge of the EGL generates a reversed flow in this region, as can be seen in Fig. 5(a), but there reaches a value of \bar{c}_s for which the magnitude of the backward velocity no longer increases since it could be said that there is a point at which the increase in the electric charge of the EGL in turn affects the concentration of ions and an equilibrium is reached between the convective and diffusive terms. Increasing velocities or streaming potential is unnecessary to maintain a zero electric current. It also shows the variation with respect to the Hartmann number, where a significant increase of B is obtained for smaller values.

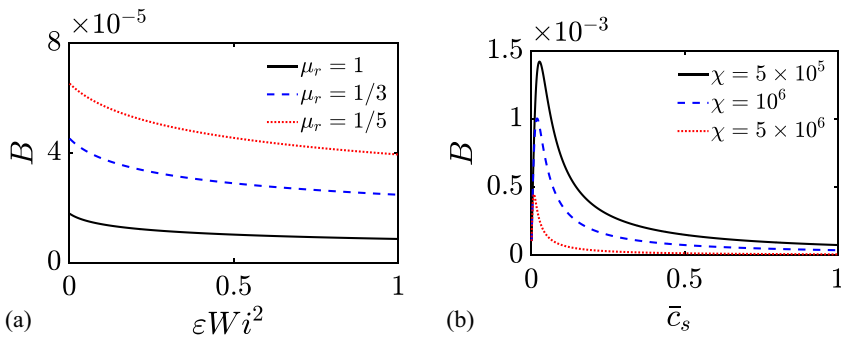


FIG. 10. Variation of the streaming potential as a function of (a) εWi^2 for three different values of μ_r with $\chi = 10^6$ and (b) \bar{c}_s varying the values of χ for $\mu_r = 1/3$. In (a) and (b), we use $\bar{\kappa} = 100$, $\xi = 250$, $\Phi = 0.01$, $\Lambda = 0.2$, $Pe_+ = 3$, and $Pe_- = 2$.

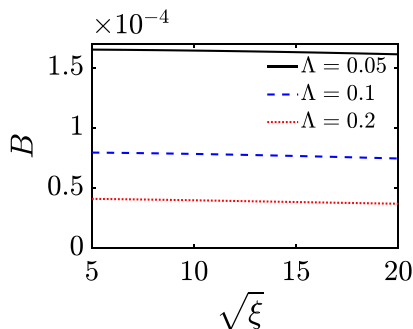


FIG. 11. Streaming potential variation with respect to $\sqrt{\xi}$ for various values of Λ with $\varepsilon\text{Wi}^2 = 0.1$, $\bar{c}_s = 1$, $\bar{\kappa} = 100$, $\Phi = 0.01$, $\mu_r = 1$, $\gamma = 0.02$, $\text{Pe}_+ = 3$, $\text{Pe}_- = 2$, and $\chi = 10^6$.

Figure 11 shows the behavior of B for different values against $\sqrt{\xi}$ for different EGL Λ thicknesses. The variation of B as a function of the permeability is almost null since slightly lower values of B are obtained for lower permeability. In general, it is possible to appreciate that, as the thickness of the EGL decreases, the streaming potential increases.

Finally, Fig. 12 shows the longitudinal variation due to the undulations of the flow potential $B_T = B + \gamma B_{\text{ind}}$. B_{ind} varies sinusoidally due to wall undulations that affect the velocity and ion distributions in the EGL.

E. Wall shear stresses

The shear stresses in the EGL are vital due to their mechanical-transductive nature, especially the stresses in the wall. The results show the effect of four important parameters according to the results shown previously, εWi^2 , \bar{c}_s , ξ , and Λ , on the stresses in the wall of the microchannel $\bar{y} = 1 + \gamma \sin(4\pi\bar{x})$. All the stresses shown are affected by the undulations up to $O(\gamma)$, so it is also possible to analyze the effect of the undulations in each of them. Figure 13 shows the viscoelastic effect on the channel wall's fluid and solid phase stresses. The Newtonian case induces the most significant magnitudes of stresses in the wall for both phases, while increasing εWi^2 said stresses decrease their magnitude, which has already been mentioned before that is due to the shear thinning effect of the viscoelastic fluid that reduces the stresses that occur at the interface compared to the Newtonian case, which are transmitted to the fluid phase and the solid phase of the EGL. Comparing the $\varepsilon\text{Wi}^2 = 1$ case with the Newtonian case, the magnitude of the stresses is almost halved for both phases. According to Figs. 4(a) and 7(a), the viscoelastic effect in the lumen affects the EGL as they

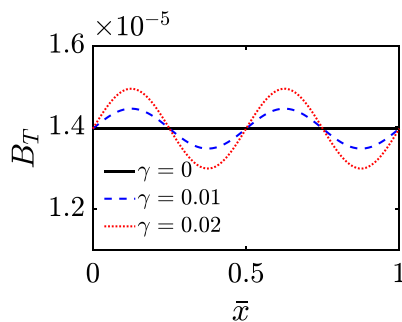


FIG. 12. Streaming potential variation (considering B_{ind}) with respect to \bar{x} for various values of γ with $\Lambda = 0.2$, $\varepsilon\text{Wi}^2 = 0.1$, $\bar{c}_s = 1$, $\bar{\kappa} = 100$, $\xi = 250$, $\Phi = 0.01$, $\mu_r = 1$, $\text{Pe}_+ = 3$, $\text{Pe}_- = 2$, and $\chi = 10^6$.

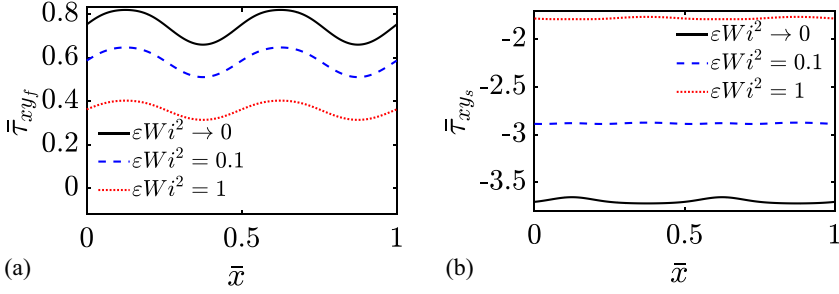


FIG. 13. Shear stresses of the fluid phase and the solid phase of the EGL in the microchannel wall ($\bar{y} = 1 + \gamma \sin 4\pi\bar{x}$) for different values of εWi^2 , with $\bar{c}_s = 1$, $\xi = 250$, $\Lambda = 0.2$, $\chi = 10^6$, $\bar{\kappa} = 100$, $\gamma = 0.02$, $\Phi = 0.01$, $\mu_r = 1$, $Pe_+ = 3$, and $Pe_- = 2$.

are coupled at the interface, reducing the magnitude and velocity gradients and deformations and generating less stress in the wall. Figure 14 shows the effect of the dimensionless electric charge in the EGL on the fluid and solid phase stresses on the channel wall. In the case of no electric charge ($\bar{c}_s \rightarrow 0$), the stresses are smaller; however, when there is a value for the charge, these stresses increase in magnitude due to the contribution of the electric stresses. Furthermore, the effects of permeability on the shear stresses of the wall are shown in Fig. 15. In the cases where the EGL has the higher permeability, the magnitudes of the larger stresses are larger than those with low permeability. The above can be explained because the fluid that flows through the EGL is the cause of the stresses that are induced in this region. Therefore, the fluid flows more freely in a material with high permeability (lower ξ), inducing higher stresses than in an impermeable limiting case ($\xi \rightarrow \infty$) where stresses would not exist in the EGL since the fluid could not penetrate the solid. The effect of the thickness of the EGL is shown in Fig. 16 and it is possible to appreciate that, for thinner EGLs, the magnitude of the stresses for the solid phase in the wall is slightly higher and for the fluid phase slightly lower compared to a thicker EGL. Finally, the effect that undulations have in general is more noticeable in the stresses of the fluid phase than in the stresses of the solid phase, according to the results shown, in addition to the fact that they tend to have a behavior more similar to the shape of the wall (sinusoidal). Some parameters can cause the stresses to be more sensitive to undulations, as in Fig. 14 where in the fluid phase the electric charge causes the stresses to have a larger longitudinal variation compared to the case $\bar{c}_s \rightarrow 0$; however, for the stresses in the solid phase the effect is the opposite.

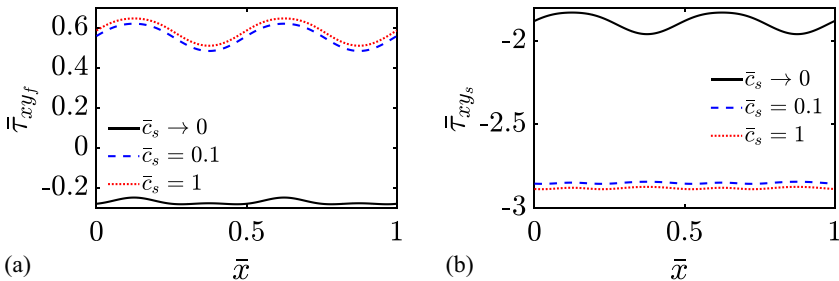


FIG. 14. Shear stresses of the fluid phase and the solid phase of the EGL in the microchannel wall ($\bar{y} = 1 + \gamma \sin 4\pi\bar{x}$) for different values of \bar{c}_s , with $\varepsilon Wi^2 = 0.1$, $\xi = 250$, $\Lambda = 0.2$, $\chi = 10^6$, $\bar{\kappa} = 100$, $\gamma = 0.02$, $\Phi = 0.01$, $\mu_r = 1$, $Pe_+ = 3$, and $Pe_- = 2$.

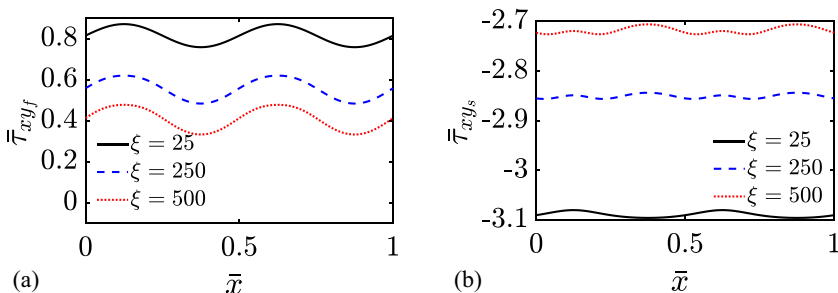


FIG. 15. Shear stresses of the fluid phase and the solid phase of the EGL in the microchannel wall ($\bar{y} = 1 + \gamma \sin 4\pi\bar{x}$) for different values of ξ , with $\varepsilon\text{Wi}^2 = 0.1$, $\bar{c}_s = 1$, $\Lambda = 0.2$, $\chi = 10^6$, $\bar{\kappa} = 100$, $\gamma = 0.02$, $\Phi = 0.01$, $\mu_r = 1$, $\text{Pe}_+ = 3$, and $\text{Pe}_- = 2$.

IV. CONCLUSIONS

The present study asymptotically analyzes the electric potential, velocity, and displacement fields through a microchannel with wavy walls and a region that covers the wall called the EGL, which is porous and electrically charged. Furthermore, we consider that the fluid outside the EGL is a non-Newtonian fluid that obeys the Phan-Thien-Tanner model.

The Poisson-Boltzmann and momentum equations were used to determine the electric field and fluid hydrodynamics all over the microchannel. During the nondimensionalization of the mathematical model, some parameters arise which characterize the studied phenomenon: the Weissenberg number εWi^2 related to the viscoelasticity of the fluid, the dimensionless electric charge of the EGL, \bar{c}_s , that encompasses the electrical effects developed in the phenomenon, the inverse of porosity ξ that represents the porous effect of the EGL, and the dimensionless thickness of the undulations, γ , disturbance parameter in the domain perturbation method. Once the distribution of the electric potential and the velocity and displacement fields are known, it is possible to analyze the induced potential streaming, which is of particular interest to know its magnitude and behavior as a possible source of energy and the stresses in the wall that allow us to understand the mechanical-transductive nature of the EGL.

The viscoelastic effect reduces the streaming potential and increases significantly with the reduction of the Hartmann number. One reason for the relationship between B and εWi^2 is due to the shear thinning that the viscoelastic fluid presents that reduces the shear stresses at the interface compared to a Newtonian fluid that are transmitted to the fluid and solid phases of the EGL and are related to the velocities of said region. On the other hand, the effect of \bar{c}_s is more challenging to describe since if $\bar{c}_s = 0$, there is no induced potential, but for small \bar{c}_s the induced potential

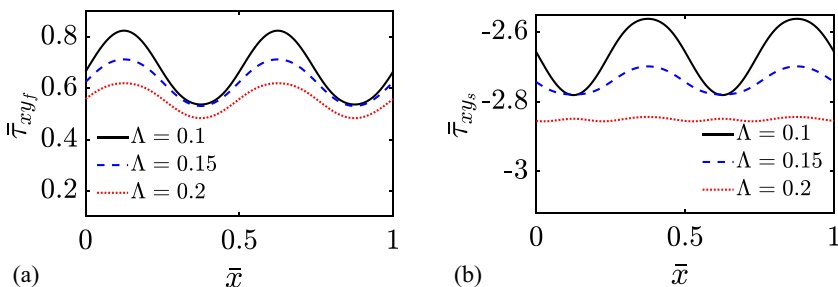


FIG. 16. Shear stresses of the fluid phase and the solid phase of the EGL in the microchannel wall ($\bar{y} = 1 + \gamma \sin 4\pi\bar{x}$) for different values of Λ , with $\varepsilon\text{Wi}^2 = 0.1$, $\bar{c}_s = 1$, $\xi = 250$, $\chi = 10^6$, $\bar{\kappa} = 100$, $\gamma = 0.02$, $\Phi = 0.01$, $\mu_r = 1$, $\text{Pe}_+ = 3$, and $\text{Pe}_- = 2$.

grows to a maximum point and then decreases in such a way that for higher values the induced potential is practically constant. However, it is not possible to establish the exact value at which these changes occur since they depend on the values of the other parameters involved. The flow potential that is induced for different configurations is approximately of the order $\sim 10^{-4}$ – 10^{-5} , that in physical variables, considering $\sim \frac{k_b T}{eH} \sim 10^4$ V/m, is approximately $\sim O(1-10^{-1})$. With the relevant technological development, the above means that it may be an option to be used as a biocompatible energy source for small devices that require electric potential values around 1 V.

The shear forces in the wall were also studied, finding that the viscoelastic effect decreases its magnitude, as previously explained, while the electric charge of the EGL and the permeability increase them. Decreasing the thickness of the EGL increases the stresses in the solid phase but decreases the magnitude of the stresses in the solid phase. The fluid phase stresses presented a higher sensitivity to wall undulations than the solid phase stresses. These relationships can help understand the relationship between certain conditions and the human body's response to them.

It should be noted that one of the advantages obtained from this work over similar numerical works is that the solution obtained can be replicated with any calculation processor; obtained solutions involve low processing and computational time, going from weeks of computation (according to what is reported in the state of the art) to a few seconds, obtaining the same results and behaviors, under the assumptions made.

The asymptotic analysis has two limitations. It is valid for shallow channels, and the amplitude of the undulations is small with respect to the width of the channel. Any analysis outside of these two limitations is outside the solutions presented here. One of the possible future works related to this work concerns a full numerical solution that is not limited to the assumptions made here, such as the slenderness of the channel or the small undulations, which can help to find the limit in which the found solution is valid.

ACKNOWLEDGMENTS

C.T. acknowledges the support from Instituto Politécnico Nacional and CONACYT programs for the Ph.D. fellowship at SEPI-ESIME-IPN. This work was supported by the Secretaría de Investigación y Posgrado, Instituto Politécnico Nacional Research Grants No. 20232096 and No. 20230206.

APPENDIX: CONSTANTS

1. Constants at the $O(\gamma^0)$ solution

Following are constants at the $O(\gamma^0)$ solution:

$$C_{pL} = -\frac{\bar{c}_s}{2(\coth(\bar{\kappa}(1-\Lambda)) + \coth(\bar{\kappa}\Lambda)) \sinh(\bar{\kappa}(1-\Lambda))}, \quad (\text{A1})$$

$$C_{pf} = \frac{\bar{c}_s}{2(\coth(\bar{\kappa}(1-\Lambda)) + \coth(\bar{\kappa}\Lambda)) \sinh(\bar{\kappa}\Lambda)}. \quad (\text{A2})$$

$$A_{11} = \mu_r^3 \frac{\varepsilon \text{Wi}^2 (1-\Lambda)^4}{2}, \quad A_{12} = \mu_r \frac{(1-\Lambda)^2}{2} + \frac{1}{\xi}, \quad A_{13} = \frac{\chi \bar{c}_s}{\xi} - \frac{2\chi C_{pf}}{\xi - \bar{\kappa}^2} \cosh \bar{\kappa} \Lambda, \quad (\text{A3})$$

$$A_{14} = -\exp(\sqrt{\xi} \Lambda), \quad A_{15} = -\exp(-\sqrt{\xi} \Lambda), \quad A_{22} = 1 - \Lambda, \quad (\text{A4})$$

$$A_{23} = \bar{\kappa} \frac{2\chi C_{pf}}{\xi - \bar{\kappa}^2} \sinh \bar{\kappa} \Lambda, \quad A_{24} = \sqrt{\xi} \exp(\sqrt{\xi} \Lambda), \quad A_{25} = -\sqrt{\xi} \exp(-\sqrt{\xi} \Lambda), \quad (\text{A5})$$

$$A_{32} = -\frac{1}{\xi}, \quad A_{33} = -\frac{\chi \bar{c}_s}{\xi} + \frac{2\chi C_{pf}}{\xi - \bar{\kappa}^2}, \quad A_{34} = 1, \quad A_{35} = 1, \quad A_{42} = \frac{2C_{pf}}{\xi \bar{\kappa}} \sinh \bar{\kappa} \Lambda - \frac{\bar{c}_s \Lambda}{\xi}, \quad (\text{A6})$$

$$A_{43} = \frac{2\chi\bar{c}_s C_{pf}}{\xi\bar{\kappa}} \sinh(\bar{\kappa}\Lambda) - \frac{\chi\bar{c}_s^2\Lambda}{\xi} - \frac{\chi C_{pf}^2}{\bar{\kappa}(\xi - \bar{\kappa}^2)} (\sinh(2\bar{\kappa}\Lambda) + 2\bar{\kappa}\Lambda) + \frac{2\chi\bar{c}_s C_{pf}}{\bar{\kappa}(\xi - \bar{\kappa}^2)} \sinh(\bar{\kappa}\Lambda) - \frac{1}{\text{Pe}_+\text{Pe}_-} \left[\Lambda(\text{Pe}_+ + \text{Pe}_-) + \frac{C_{pf}(\text{Pe}_+ - \text{Pe}_-)}{\bar{\kappa} \sinh(\bar{\kappa}\Lambda)} + \frac{\bar{c}_s(\text{Pe}_m - \text{Pe}_+)\Lambda}{2} \right], \quad (\text{A7})$$

$$A_{44} = \frac{\bar{c}_s(\exp(\sqrt{\xi}\Lambda) - 1)}{\sqrt{\xi}} - 2C_{pf} \frac{\exp(\sqrt{\xi}\Lambda)(\sqrt{\xi} \cosh(\bar{\kappa}\Lambda) - \bar{\kappa} \sinh \bar{\kappa}\Lambda) - \sqrt{\xi}}{\xi - \bar{\kappa}^2}, \quad (\text{A8})$$

$$A_{45} = -\frac{\bar{c}_s(\exp(-\sqrt{\xi}\Lambda) - 1)}{\sqrt{\xi}} + 2C_{pf} \frac{\exp(-\sqrt{\xi}\Lambda)(\sqrt{\xi} \cosh(\bar{\kappa}\Lambda) + \bar{\kappa} \sinh \bar{\kappa}\Lambda) - \sqrt{\xi}}{\xi - \bar{\kappa}^2}, \quad (\text{A9})$$

$$A_{112} = A_{12} - \frac{A_{15}A_{42}}{A_{45}} - \left(A_{14} - \frac{A_{15}A_{44}}{A_{45}} \right) \frac{A_{32} - \frac{A_{35}A_{42}}{A_{45}}}{A_{34} - \frac{A_{35}A_{44}}{A_{45}}}, \quad (\text{A10})$$

$$A_{113} = A_{13} - \frac{A_{15}A_{43}}{A_{45}} - \left(A_{14} - \frac{A_{15}A_{44}}{A_{45}} \right) \frac{A_{33} - \frac{A_{35}A_{43}}{A_{45}}}{A_{34} - \frac{A_{35}A_{44}}{A_{45}}}, \quad (\text{A11})$$

$$A_{122} = A_{22} - \frac{A_{25}A_{42}}{A_{45}} - \left(A_{24} - \frac{A_{25}A_{44}}{A_{45}} \right) \frac{A_{32} - \frac{A_{35}A_{42}}{A_{45}}}{A_{34} - \frac{A_{35}A_{44}}{A_{45}}}, \quad (\text{A12})$$

$$A_{123} = A_{23} - \frac{A_{25}A_{43}}{A_{45}} - \left(A_{24} - \frac{A_{25}A_{44}}{A_{45}} \right) \frac{A_{33} - \frac{A_{35}A_{43}}{A_{45}}}{A_{34} - \frac{A_{35}A_{44}}{A_{45}}}, \quad (\text{A13})$$

$$A_{00} = A_{112} - A_{113} \frac{A_{122}}{A_{123}}. \quad (\text{A14})$$

$$G = \frac{(\sqrt{3}\sqrt{27A_{11}^4 + 4A_{11}^3A_{00}^3 - 9A_{11}^2})^{1/3}}{(18^{1/3})A_{11}} - \frac{(2/3)^{1/3}A_{00}}{(\sqrt{3}\sqrt{27A_{11}^4 + 4A_{11}^3A_{00}^3 - 9A_{11}^2})^{1/3}}, \quad (\text{A15})$$

$$B = -\frac{A_{122}}{A_{123}}G, \quad (\text{A16})$$

$$C_{f1} = \frac{-(A_{32} - \frac{A_{35}A_{42}}{A_{45}})G - (A_{33} - \frac{A_{35}A_{43}}{A_{45}})B}{A_{34} - \frac{A_{35}A_{44}}{A_{45}}}, \quad (\text{A17})$$

$$C_{f2} = -\frac{A_{42}}{A_{45}}G - \frac{A_{43}}{A_{45}}B - \frac{A_{44}}{A_{45}}C_{f1}. \quad (\text{A18})$$

$$C_{u1} = -G(\Phi + \Lambda) + \frac{2\xi B\chi C_{pf}}{\bar{\kappa}(\xi - \bar{\kappa}^2)} \sinh(\bar{\kappa}\Lambda) + C_{f1}\sqrt{\xi} \exp(\sqrt{\xi}\Lambda) - C_{f2}\sqrt{\xi} \exp(-\sqrt{\xi}\Lambda), \quad (\text{A19})$$

$$C_{u2} = \frac{2\xi B\chi C_{pf}}{\bar{\kappa}^2(\xi - \bar{\kappa}^2)} + C_{f1} + C_{f2}. \quad (\text{A20})$$

2. Constants at the $O(\gamma)$ solution

Following are constants at the $O(\gamma)$ solution:

$$C_{g3} = \bar{\kappa}C_{pf} \sin(4\pi\bar{x}). \quad (\text{A21})$$

$$C_{g1} = \frac{\bar{\kappa}(C_{pf} \cosh(\bar{\kappa}\Lambda) - C_{pL} \cosh(\bar{\kappa}(1-\Lambda))) \sin(4\pi\bar{\kappa})}{\sinh(\bar{\kappa}(1-\Lambda)) + \cosh(\bar{\kappa}(1-\Lambda)) \tanh(\bar{\kappa}\Lambda)} - \frac{C_{g3}(\cosh(\bar{\kappa}\Lambda) - \tanh(\bar{\kappa}\Lambda) \sinh(\bar{\kappa}\Lambda))}{\sinh(\bar{\kappa}(1-\Lambda)) + \cosh(\bar{\kappa}(1-\Lambda)) \tanh(\bar{\kappa}\Lambda)}, \quad (\text{A22})$$

$$C_{g2} = C_{g1} \frac{\cosh(\bar{\kappa}(1-\Lambda))}{\cosh(\bar{\kappa}\Lambda)} - C_{g3} \tanh(\bar{\kappa}\Lambda), \quad (\text{A23})$$

$$C_{300} = \bar{\kappa}C_{pf}, \quad (\text{A24})$$

$$C_{100} = \frac{(\bar{\kappa}(C_{pf} \cosh(\bar{\kappa}\Lambda) - C_{pL} \cosh(\bar{\kappa}(1-\Lambda))) - C_{300}(\cosh(\bar{\kappa}\Lambda) - \tanh(\bar{\kappa}\Lambda) \sinh(\bar{\kappa}\Lambda)))}{\sinh(\bar{\kappa}(1-\Lambda)) + \cosh(\bar{\kappa}(1-\Lambda)) \tanh \bar{\kappa}\Lambda}, \quad (\text{A25})$$

$$C_{200} = C_{100} \frac{\cosh(\bar{\kappa}(1-\Lambda))}{\cosh(\bar{\kappa}\Lambda)} - C_{300} \tanh(\bar{\kappa}\Lambda), \quad (\text{A26})$$

$$C_{500} = \left\{ \frac{1}{-\sqrt{\xi} \exp(-\sqrt{\xi}\Lambda)} \left(\bar{\kappa} \frac{2\chi BC_{200}}{\xi - \bar{\kappa}^2} \sinh(\bar{\kappa}\Lambda) + (\bar{\kappa}C_{300} - \bar{\kappa}^2 C_{pf}) \frac{2\chi B}{\xi - \bar{\kappa}^2} \cosh(\bar{\kappa}\Lambda) - C_{f1}\xi \exp(\sqrt{\xi}\Lambda) - C_{f2}\xi \exp(-\sqrt{\xi}\Lambda) + G \right) - \frac{2\chi BC_{200}}{\xi - \bar{\kappa}^2} + (C_{f1} - C_{f2})\sqrt{\xi} \right\} / (1 + \exp(2\sqrt{\xi}\Lambda)), \quad (\text{A27})$$

$$C_{501} = \left\{ \frac{1}{-\sqrt{\xi} \exp(-\sqrt{\xi}\Lambda)} \left(\frac{2\chi C_{pf}}{\xi - \bar{\kappa}^2} (\bar{\kappa} \sinh(\bar{\kappa}\Lambda) - 1) + \frac{\chi \bar{c}_s}{\xi} \right) \right\} / (1 + \exp(2\sqrt{\xi}\Lambda)), \quad (\text{A28})$$

$$C_{502} = \left\{ \frac{1}{-\sqrt{\xi} \exp(-\sqrt{\xi}\Lambda)} (1 - \Lambda) + \frac{1}{\xi} \right\} / (1 + \exp(2\sqrt{\xi}\Lambda)), \quad (\text{A29})$$

$$C_{600} = \left\{ -\sqrt{\xi} \exp(\sqrt{\xi}\Lambda) C_{500} - \left(\bar{\kappa} \frac{2\chi Bc_{200}}{\xi - \bar{\kappa}^2} \sinh(\bar{\kappa}\Lambda) + (\bar{\kappa}C_{300} - \bar{\kappa}^2 C_{pf}) \frac{2B\chi}{\xi - \bar{\kappa}^2} \cosh(\bar{\kappa}\Lambda) - C_{f1}\xi \exp(\sqrt{\xi}\Lambda) - C_{f2}\xi \exp(-\sqrt{\xi}\Lambda) + G \right) / (-\sqrt{\xi} \exp(-\sqrt{\xi}\Lambda)) \right\} \quad (\text{A30})$$

$$C_{601} = \left\{ -\sqrt{\xi} \exp(\sqrt{\xi}\Lambda) C_{501} - \bar{\kappa} \frac{2\chi C_{pf}}{\xi - \bar{\kappa}^2} \sinh(\bar{\kappa}\Lambda) \right\} / (-\sqrt{\xi} \exp(-\sqrt{\xi}\Lambda)) \quad (\text{A31})$$

$$C_{602} = \{-\sqrt{\xi} \exp(\sqrt{\xi}\Lambda) C_{502} - (1 - \Lambda)\} / (-\sqrt{\xi} \exp(-\sqrt{\xi}\Lambda)), \quad (\text{A32})$$

$$C_{400} = C_{500} \exp(\sqrt{\xi}\Lambda) + C_{600} \exp(-\sqrt{\xi}\Lambda) + (C_{300} - \bar{\kappa}C_{pf}) \frac{2\chi B}{\xi - \bar{\kappa}^2} \sinh(\bar{\kappa}\Lambda) + \frac{2\chi BC_{200}}{\xi - \bar{\kappa}^2} \cosh(\bar{\kappa}\Lambda) - C_{f1}\sqrt{\xi} \exp(\sqrt{\xi}\Lambda) + C_{f2}\sqrt{\xi} \exp(-\sqrt{\xi}\Lambda) - (1 + 2\varepsilon W i^2 \mu_r^2 G^2 (1 - \Lambda)^2) \mu_r G (1 - \Lambda), \quad (\text{A33})$$

$$C_{401} = C_{501} \exp(\sqrt{\xi}\Lambda) + C_{601} \exp(-\sqrt{\xi}\Lambda) - \frac{\chi \bar{c}_s}{\xi} + \frac{2\chi C_{pf}}{\xi - \bar{\kappa}^2} \cosh(\bar{\kappa}\Lambda), \quad (\text{A34})$$

$$C_{402} = C_{502} \exp(\sqrt{\xi} \Lambda) + C_{602} \exp(-\sqrt{\xi} \Lambda) - \frac{\mu_r(1-\Lambda)^2}{2} (1 + 3\varepsilon \text{Wi}^2 \mu_r G^2 (1-\Lambda)^2) - \frac{1}{\xi}, \quad (\text{A35})$$

$$\alpha_1 = 3\varepsilon \text{Wi}^2 \mu_r^2 G^2, \quad \alpha_2 = \frac{2\chi BC_{200}}{\xi - \bar{\kappa}^2}, \quad \alpha_3 = \frac{2\chi C_{pf}}{\xi - \bar{\kappa}^2}, \quad (\text{A36})$$

$$\alpha_4 = \frac{2\chi BC_{300}}{\xi - \bar{\kappa}^2}, \quad \alpha_5 = -\frac{\chi \bar{c}_s}{\xi}, \quad \alpha_6 = -\frac{1}{\xi}, \quad (\text{A37})$$

$$\psi_{f10}(\bar{y}) = C_{200} \cosh(\bar{\kappa}(1-\bar{y})) + C_{g300} \sinh(\bar{\kappa}(1-\bar{y})), \quad (\text{A38})$$

$$\bar{c}_{f\pm 10}(\bar{y}) \approx \mp \bar{\psi}_{f10}(\bar{y}), \quad (\text{A39})$$

$$\bar{c}_{f\pm 10}(\bar{y}) \approx \mp \bar{\psi}_{f10}(\bar{y}), \quad (\text{A40})$$

$$\bar{v}_{Lx10}(B_{\text{ind}0}, G_{\text{ind}0}, \bar{y}) = \frac{\mu_r G_{\text{ind}0} \bar{y}^2}{2} (1 + \alpha_1 \bar{y}^2) + C_{400} + B_{\text{ind}0} C_{401} + G_{\text{ind}0} C_{402}, \quad (\text{A41})$$

$$\begin{aligned} \bar{v}_{fx10}(B_{\text{ind}0}, G_{\text{ind}0}, \bar{y}) &= (\alpha_2 + B_{\text{ind}0} \alpha_3) \cosh(\bar{\kappa}(1-\bar{y})) + \alpha_4 \sinh(\bar{\kappa}(1-\Lambda)) \\ &+ B_{\text{ind}0} \alpha_5 + G_{\text{ind}0} \alpha_6 + (C_{500} + B_{\text{ind}0} C_{501} + G_{\text{ind}0} C_{502}) \exp(\sqrt{\xi} \bar{y}) \\ &+ (C_{600} + B_{\text{ind}0} C_{601} + G_{\text{ind}0} C_{602}) \exp(-\sqrt{\xi} \bar{y}), \end{aligned} \quad (\text{A42})$$

$$C_{g4} = C_{400} \sin(4\pi \bar{x}) + C_{401} B_{\text{ind}} + C_{402} G_{\text{ind}}, \quad (\text{A43})$$

$$C_{g5} = C_{500} \sin(4\pi \bar{x}) + C_{501} B_{\text{ind}} + C_{502} G_{\text{ind}}, \quad (\text{A44})$$

$$C_{g6} = C_{600} \sin(4\pi \bar{x}) + C_{601} B_{\text{ind}} + C_{602} G_{\text{ind}}. \quad (\text{A45})$$

$$\begin{aligned} C_{g7} &= \frac{2\chi \xi (B_{\text{ind}} C_{pf} + BC_{g2})}{\bar{\kappa}(\xi - \bar{\kappa}^2)} \sinh(\bar{\kappa} \Lambda) + \frac{2B\chi \xi C_{g3}}{\bar{\kappa}(\xi - \bar{\kappa}^2)} \cosh(\bar{\kappa} \Lambda) + C_{g5} \sqrt{\xi} \exp(\sqrt{\xi} \Lambda) \\ &- C_{g6} \sqrt{\xi} \exp(-\sqrt{\xi} y^*) - G_{\text{ind}}(\Phi + \Lambda) - \left(-G + \frac{2\xi B\chi C_{pf}}{\xi - \bar{\kappa}^2} \cosh(\bar{\kappa} \Lambda) \right. \\ &\left. + \xi C_{f1} \exp(\sqrt{\xi} y^*) + \xi C_{f2} \exp(-\sqrt{\xi} y^*) \right) \sin(4\pi \bar{x}), \end{aligned} \quad (\text{A46})$$

$$C_{g8} = \frac{2\chi \xi (B_{\text{ind}} C_{pf} + BC_{g2})}{\bar{\kappa}^2(\xi - \bar{\kappa}^2)} + C_{g5} + C_{g6} + (\sqrt{\xi}(C_{f2} - C_{f1}) + C_{u1}) \sin(4\pi \bar{x}). \quad (\text{A47})$$

-
- [1] A. R. Pries, T. W. Secomb, and P. Gaehtgens, The endothelial surface layer, *Pflug. Arch. Eur. J. Physiol.* **440**, 653 (2000).
- [2] A. C. Frati-Munari, Importancia médica del glucocáliz endotelial, *Arch. Cardiol. Mex.* **83**, 303 (2013).
- [3] E. R. Damiano and T. M. Stace, Flow and deformation of the capillary glycocalyx in the wake of a leukocyte, *Phys. Fluids* **17**, 031509 (2005).
- [4] S. Weinbaum, J. M. Tarbell, and E. R. Damiano, The structure and function of the endothelial glycocalyx layer, *Annu. Rev. Biomed. Eng.* **9**, 121 (2007).
- [5] D. S. Hariprasad and T. W. Secomb, Motion of red blood cells near microvessel walls: Effects of a porous wall layer, *J. Fluid Mech.* **705**, 195 (2012).

-
- [6] E. R. Damiano, B. R. Duling, K. Ley, and T. C. Skalak, Axisymmetric pressure-driven flow of rigid pellets through a cylindrical tube lined with a deformable porous wall layer, *J. Fluid Mech.* **314**, 163 (1996).
- [7] H. H. Wei, S. L. Waters, S. Q. Liu, and J. B. Grotberg, Flow in a wavy-walled channel lined with a poroelastic layer, *J. Fluid Mech.* **492**, 23 (2003).
- [8] P. P. Sumets, J. E. Caterm, D. S. Long, and R. J. Clarke, A boundary-integral representation for biphasic mixture theory, with application to the post-capillary glycocalyx, *Proc. R. Soc. London* **471**, 20140955 (2015).
- [9] T. C. Lee, D. S. Long, and R. J. Clarke, Effect of endothelial glycocalyx layer redistribution upon microvessel poroelastohydrodynamics, *J. Fluid Mech.* **798**, 812 (2016).
- [10] A. Silberberg, Polyelectrolytes at the endothelial cell surface, *Biophys. Chem.* **41**, 9 (1991).
- [11] M. Liu and J. Yang, Electrokinetic effect of the endothelial glycocalyx layer on two-phase blood flow in small blood vessels., *Microvasc. Res.* **78**, 14 (2009).
- [12] T. M. Stace and E. R. Damiano, An electrochemical model of the transport of charged molecules through the capillary glycocalyx, *Biophys. J.* **80**, 1670 (2001).
- [13] M. D. Buschmann and A. J. Grodzinsky, A molecular model of proteoglycan-associated electrostatic forces in cartilage mechanics, *Trans. ASME J. Biomech. Engng* **117**, 179 (1995).
- [14] A. J. Mokady, A. J. Mestel, and C. P. Winlove, Flow through a charged biopolymer layer, *J. Fluid Mech.* **383**, 353 (1999).
- [15] E. R. Damiano and T. M. Stace, A mechano-electrochemical model of radial deformation of the capillary glycocalyx, *Biophys. J.* **82**, 1153 (2002).
- [16] P. P. Sumets, J. E. Caterm, D. S. Long, and R. J. Clarke, Electro-poroelastohydrodynamics of the endothelial glycocalyx layer, *J. Fluid Mech.* **838**, 284 (2018).
- [17] R. Roy, S. Mukherjee, R. Lakkaraju, and S. Chakraborty, Streaming potential in bio-mimetic microvessels mediated by capillary glycocalyx, *Microvasc. Res.* **132**, 104039 (2020).
- [18] R. F. Probstein, *Physicochemical Hydrodynamics* (Springer, Berlin, 1994).
- [19] D. A. Nield and A. Bejan, *Convection in Porous Media* (Springer, Berlin, 2006).
- [20] N. Phan-Thien and R. I. Tanner, A new constitutive equation derived from network theory, *J. Non-Newtonian Fluid Mech.* **2**, 353 (1977).
- [21] J. H. Masliyah and S. hattacharjee, *Electrokinetic and Colloid Transport Phenomena* (John Wiley & Sons, New York, 2006).
- [22] S. R. Gorthi, H. S. Gaikwad, P. K. Mondal, and G. Biswas, Surface tension driven filling in a soft microchannel: Role of streaming potential, *Ind. Eng. Chem. Res.* **59**, 3839 (2020).
- [23] L. G. Leal, *Advanced Transport Phenomena* (Cambridge University Press, Cambridge, UK, 2007).
- [24] M. Brust, C. Schaefer, R. Doerr, L. Pan, M. Garcia, P. E. Arratia, and C. Wagner, Rheology of human blood plasma: Viscoelastic versus Newtonian behavior, *Phys. Rev. Lett.* **110**, 078305 (2013).
- [25] L. F. Delgadillo, G. A. Marsh, and R. E. Waugh, Endothelial glycocalyx layer properties and its ability to limit leukocyte adhesion, *Biophys. J.* **118**, 1564 (2020).